Quantifying groundwater exploitation induced subsidence in the Rafsanjan Plain, southeastern Iran, using InSAR time-series and in situ measurements

Mahdi Motagh[1,2], Roghayeh Shamshiri[3], Mahmud Haghshenas-Haghighi[1], Hans-Ulrich Wetzel[1], Bahman Akbari[4], Hossein Nahavandchi[3], Sigrid Roessner[1] and Siavash Arabi[5]

1- GFZ German Research Centre for Geosciences, Department of Geodesy, Section of Remote Sensing, 14473 Potsdam, Germany

2- Institute for Photogrammetry and GeoInformation, Leibniz Universität Hannover, 30167 Hannover, Germany

3- Norwegian University of Science and Technology, Department of Civil and Environmental Engineering, 7491 Trondheim, Norway

4- Forest, Range and Watershed Management organization, 1955756114 Tehran, Iran

5- National Cartographic Centre of Iran (NCC), Tehran, Iran

Abstract

Decades of groundwater overexploitation for agriculture and industrial development have resulted in substantial land subsidence in the Rafsanjan plain of southeastern Iran. This work presents the results of an InSAR time series analysis obtained by the exploitation of Envisat, ALOS and Sentinel-1 (S1) SAR data archives between June, 2004, and May, 2016, to investigate land subsidence in the plain. The InSAR analysis revealed an area of approximately 1000 km^2 within the study area showing subsidence of greater than 5 cm/year and locally exceeding 20 cm/yr in the last decade. This area of significant subsidence is limited in its spatial extent to the agricultural land and is

partly influenced by Quaternary faults. The temporal and areal relationships of subsidence and groundwater level data suggest that a significant part of the observed subsidence in the Rafsanjan region is caused by intense groundwater extraction that has led to widespread compaction within the upper parts of the up to 300 m thick unconsolidated sediments, causing irreversible and inelastic deformation of the aquifer. The average volume storage loss of the aquifer system due to overexploitation is estimated to have been approximately 300 million cubic metre (mcm)/yr over the last decade.

Keywords: subsidence, InSAR, groundwater extraction, agriculture, Iran

1. Introduction

Land subsidence due to the overdrafting of groundwater resources for industrial and agricultural purposes is a geological hazard that affects many urban and agricultural areas in the world. It is well-known, for example, in Bangkok in Thailand (Phien-wej et al., 2006), Mexico City (Cabral-Cano et al., 2008), Antelope Valley, California (Galloway et al., 1998); Las Vegas Valley, Nevada (Amelung et al., 1999), Venice in Italy (Tosi et al., 2013) and Beijing in China (Chen et al., 2016). The excessive exploitation of groundwater drains the pores of aquifers, reducing the pore fluid pressure of water. This leads to an increase in the supportive effective stress on the fluid-rock system. The aquifer skeleton may then consolidate or compact due to the increase in the effective stress by the rearrangement of the grains (Terzaghi, 1925).

Several environmental effects and consequences are associated with land subsidence including damage to infrastructures and buildings (Abidin et al., 2001; Shamshiri et al., 2014), increased risk of flooding in coastal areas (Dixon et al., 2006) and accelerated

47 erosion along earth fissures and drainage systems (Conway, 2015). Monitoring the
48 spatial extent and temporal evolution of surface deformation associated with fluid
49 withdrawal is critical to mitigate hazards associated with this phenomenon (Herrera et
50 al., 2009; Huang et al., 2012).

51 Among ground and space-based geodetic methods used for measuring land subsidence
52 (Abidin et al., 2008), space-borne interferometric synthetic aperture radar (InSAR)
53 enables a unique imaging capability for the assessment of subsidence in response to
54 fluid extraction from subsurface reservoirs (Galloway et al., 1998; Teatini et al., 2005).
55 Differential Interferometric SAR (DInSAR) and advanced multi-temporal
56 interferometry methods (e.g., permanent/persistent scatterer interferometry (Ferretti et
57 al., 2001) and small baseline subsets (Berardino et al., 2002)) provide high spatial-
58 resolution (up to 25 cm) techniques for accurately (sub-centimetre to sub-millimetre
59 accuracy) mapping the temporal and spatial distribution patterns of deformation (Casu
60 et al., 2006; Ferretti et al., 2007; Manzo et al., 2012), allowing better characterizations
61 of the elastic and inelastic properties of aquifer systems with high degrees of spatial
62 resolution in both space and time (Canova et al., 2012; Ezquerro et al., 2014; Hoffmann
63 et al., 2001; Rigo et al., 2013; Tomás et al., 2010a; Tung et al., 2016). InSAR
64 measurements also help identify the influence of geological structures on spatial
65 patterns of subsidence (Bawden et al., 2001; Burbey, 2008; Calderhead et al., 2011;
66 Motagh et al., 2007; Stramondo et al., 2007).

67 Decades of extensive groundwater extraction from aquifers, which are used mainly for
68 agricultural activities, have caused substantial land subsidence in developed
69 groundwater basins across Iran that at some locations have exceeded 20-30 cm/yr
70 (Akbari and Motagh, 2012; Anderssohn et al., 2008; Davoodijam et al., 2015; Dehghani

et al., 2009; Dehghani et al., 2013; Motagh et al., 2008; Motagh et al., 2007). This study focuses on the Rafsanjan plain, which is located in the Kerman province in the southeast of Iran (Fig. 1). This area, possibly more than any other agricultural region in the country, has been adversely affected by land subsidence due to the overdrafting of groundwater resources (Rahnama and Moafi, 2009; Sayyaf et al., 2014). The ongoing pattern of land subsidence in Rafsanjan was first documented using GPS measurements (Mousavi et al., 2001). In a recent study, (Motagh et al., 2008) analysed a few space-borne C-band SAR images from Envisat using the InSAR technique and showed that the differential interferograms of this area are dominated by a plain-wide subsidence bowl that is oriented northwest-southeast along the axis of the plain and punctuated by several circular fringes exhibiting intense localized subsidence. A field investigation in 2010 carried out following that earlier study revealed that the locations of circular structures in the differential interferograms coincided with the locations of exploitation wells (Fig. 1b), which are therefore the direct consequence of the compaction around the wells resulting from overdraft conditions (Calderhead et al., 2011).

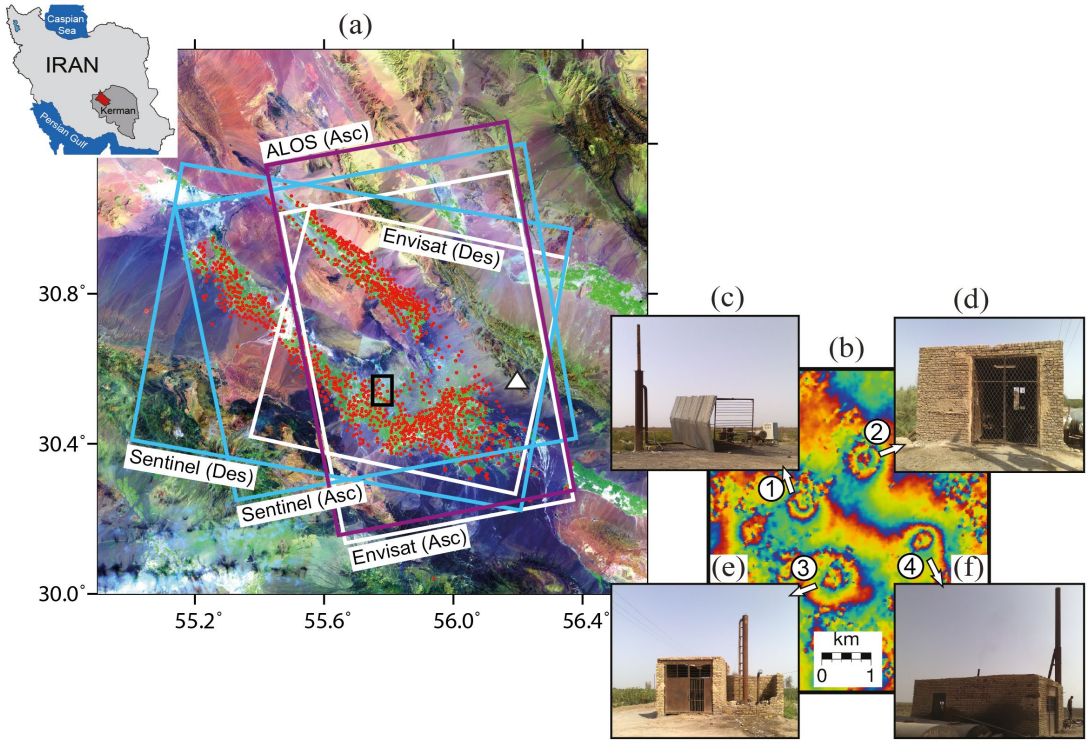

86

87 Figure 1: (a) Landsat 8 image of the study area. The inset at the top left indicates the location of Rafsanjan
88 plain in Iran. The rectangles show the frames of radar sensors used in this study; the white frames
89 correspond to Envisat tracks in descending and ascending orbits, the purple to ascending ALOS and the
90 blue to S1 tracks in ascending and descending orbits. The red dots are the locations of exploitation wells
91 in the valley. The white triangle is the location of the Davaran precipitation station. (b) A close-up view
92 of the wrapped Envisat interferogram from (Motagh et al., 2008), which spans 17 May to 26 July 2005
93 for the area marked by the black rectangle in Fig. 1*a*. (c), (d), (e) and (f) refer to the field pictures
94 depicting the 'pumping stations' located in the centre of the circular fringes in Fig. 1b. They are marked
95 by white arrows and labelled 1, 2, 3 and 4, corresponding to (c), (d), (e) and (f), respectively.

96 In this paper, we extend the earlier study of Motagh et al. (2008) by using more SAR
97 data from Envisat, ALOS and Sentinel-1 (S1) satellites and applying the multi-temporal
98 InSAR time-series analysis technique (Berardino et al., 2002; Hooper, 2008) to better
99 resolve the spatial and temporal patterns of subsidence in Rafsanjan. The use of the
100 InSAR time-series technique to monitor groundwater-induced deformation is
101 particularly relevant in areas such as Rafsanjan, where no detailed information exists

on the history of subsidence and where no ground-based geodetic monitoring system is yet operative to document the temporal and spatial pattern of ongoing land subsidence. Complimentary, InSAR-derived results are analysed in conjunction with geological maps, field inspection, and measurements of hydraulic head fluctuations to better assess hydro-geologic parameters that affect the spatio-temporal characteristics of land subsidence. Moreover, the storage properties of the aquifer system and its volume loss due to overexploitation are evaluated using the temporal relationship between InSAR-derived subsidence and artesian-head change.

2. Study area

Fig. 2 illustrates the geological setting of the Rafsanjan area. The last and main Quaternary deformation in Rafsanjan, which is located in the Yazd Block of the Central Iranian Microcontinent (CIM), led to narrow saddles and basin structures that are oriented NW-SE and controlled by complex fault systems and fracture zones (Aghanabati, 2004; Ghorbani, 2013). The resulting structure patterns are morphological antiforms (blocks of outcropping Mesozoic and older units) and synforms such as the intra-mountainous basins of Noogh-Bahreman and Koshkoueieh-Rafsanjan that are filled with sediments originating from the outcropping materials of the antiforms (talus cones, gravel fans, river sediments with terraces, dunes and sand sheets and Sabkha sediments composed of salty silts, clays and mud flats, salts and gypsum). The seismically active Darivan thrust fault (Hessami et al., 2003) marks the northern boundary of a block structure that consists of Mesozoic-Palaeozoic basement units; close to the fault, the block units are composed mainly of Devonian to Carboniferous or Cambrian sandstones, quartzite, shales, conglomerates, and lesser carbonate rocks, whereas away from the fault, the units are mainly Cretaceous limestones and clastic

126 sediments. In the south, the basin region of Noogh-Bahreman is bounded by a saddle
127 structure whose northern flank is controlled by a Quaternary NW-SE- fault system that
128 is named in this paper the Bahreman fault due to its proximity to the Bahreman village.
129 The rock units in this outcropping rock complex are subdivided into intensely fractured
130 micro-blocks that consist of several hundred metres of Upper Cretaceous (Campanian-
131 Maastrichtian) coarse-grained carbonates and sandy limestones and partly of Eocene
132 volcanics and associated sedimentary rocks. The region of Koshkoueieh-Rafsanjan,
133 which has several hundred metres of similar Quaternary basin fill, represents the basin
134 structure situated in the furthermost SW of the study area; it is bounded by the
135 Quaternary Rafsanjan strike-slip fault and the Eocene volcanics and conglomerates.
136 The aquifers in the Rafsanjan basin receive their recharge from direct precipitation,
137 seasonal river discharge, basin-wide run-off from the relatively impermeable rocks of
138 the surrounding high ranges, infiltration into faults and fractures zones, and surface
139 water infiltration through coarse grained sediments deposited in the fans. Figs. 2b-d
140 show the lithologic log descriptions for 3 hydrogeological wells and their locations in
141 the study area. As depicted in those figures, the thickness of the high permeability
142 deposits (gravels with sand) increases towards the surrounding mountain ranges. The
143 lithological profiles also indicate that the thickness of less permeable material (clay and
144 clay with interbeds of sand) increases with depth towards the centre of the plain in
145 comparison to the areas closer to the mountain range.

(a)

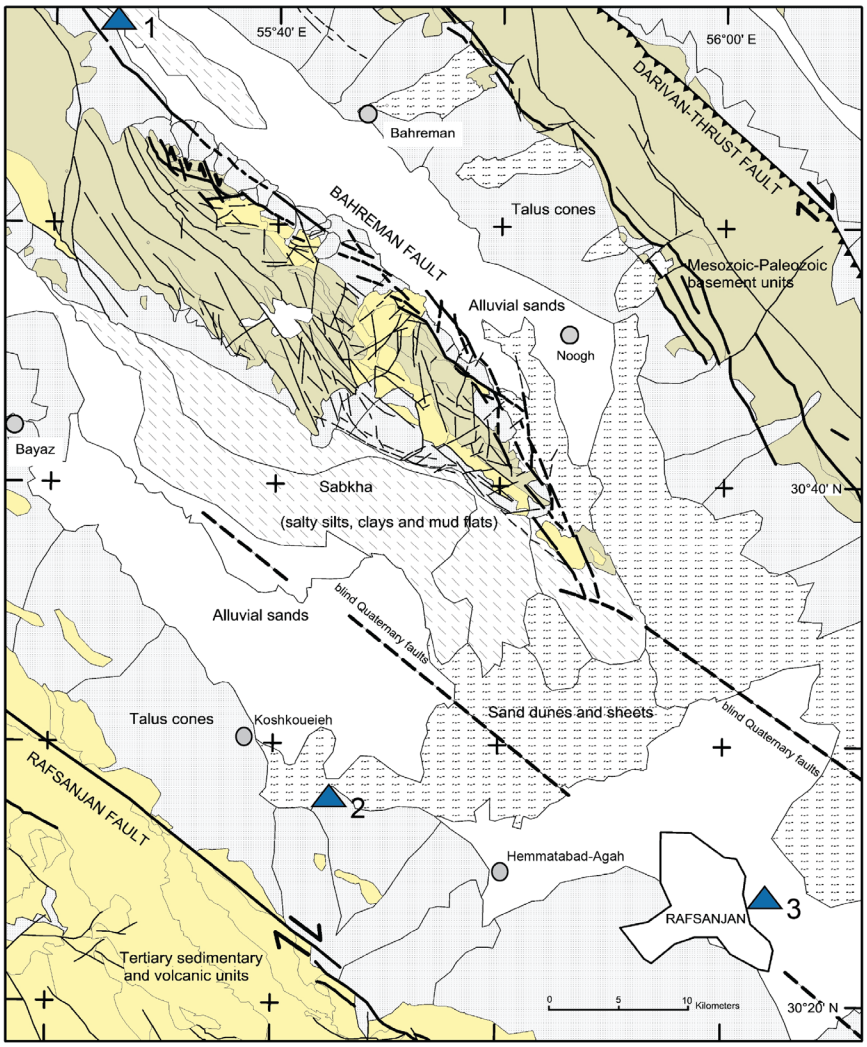
1
55°40' E
56°00' E
Bahreman
DARVAN-THRUST FAULT
BAHREMAN FAULT
Talus cones
Mesozoic-Paleozoic basement units
Alluvial sands
Noogh
Bayaz
Sabkha
30°40' N
(salty silts, clays and mud flats)
Alluvial sands
blind Quaternary faults
Talus cones
Koshkoueieh
Sand dunes and sheets
blind Quaternary faults
RAFSANJAN FAULT
2
Hemmatabad-Agah
RAFSANJAN
3
Tertiary sedimentary and volcanic units
0 5 10 Kilometers
30°20' N

(b)

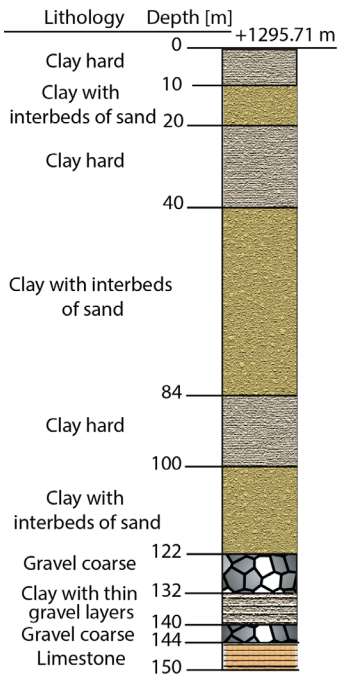
Lithology
Depth [m]
+1295.71 m
0
Clay hard
10
Clay with interbeds of sand
20
Clay hard
40
Clay with interbeds of sand
84
Clay hard
100
Clay with interbeds of sand
122
Gravel coarse
132
Clay with thin gravel layers
140
Gravel coarse
144
Limestone
150

(c)

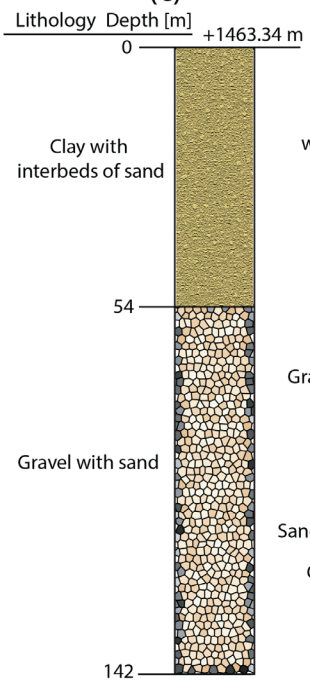
Lithology
Depth [m]
+1463.34 m
0
Clay with interbeds of sand
54
Gravel with sand
142

(d)

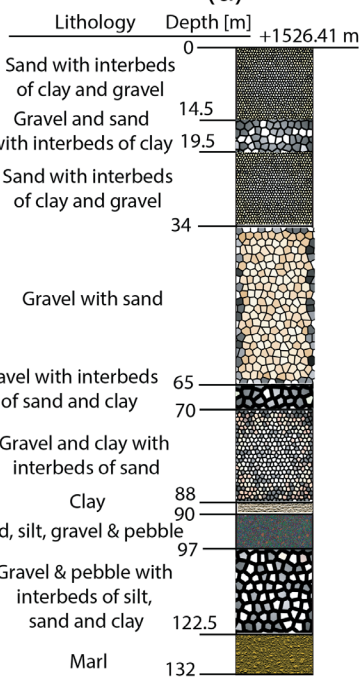
Lithology
Depth [m]
+1526.41 m
0
Sand with interbeds of clay and gravel
14.5
Gravel and sand with interbeds of clay
19.5
Sand with interbeds of clay and gravel
34
Gravel with sand
Gravel with interbeds of sand and clay
65
70
Gravel and clay with interbeds of sand
Clay
88
90
Sand, silt, gravel & pebble
97
Gravel & pebble with interbeds of silt, sand and clay
122.5
Marl
132

146

Figure 2: (a) Geological setting of the study area. The geological information is from 1:250,000 geological maps (Mahdavi, 1996; Zohrehbakhsh et al., 1992) as well as a 1:2500,000 map of (Hessami et al., 2003) and Landsat ETM data. The main townships and villages of Noogh, Bahreman, Bayaz, Koshkoueieh, and Hemmatabad-Agah are depicted by grey-filled circles. The boundary of Rafsanjan City has been marked by a black polygon. (b), (c) and (d) show lithological logs of 3 exemplary wells, which are marked by blue triangles and are numbered 1, 2, and 3 in Fig. 2a, respectively (Sayyaf et al., 2014; Zayandehroodi, 2012)

The climate of the study area is characterized as the arid and hyper-arid type, with mean annual rainfall of ~100 mm (Fig. 3) and potential evaporation of more than 3000 mm (Mehryar et al., 2015). The region is among the main producers of pistachios in the world, with more than 90% of its agricultural fields being allocated to pistachio crops. The total area of agricultural land has increased by approximately 50% in the past 3 decades, although the rate of expansion has slowed down recently due to the impact of drought and increasing water scarcity (Mehryar et al., 2015).

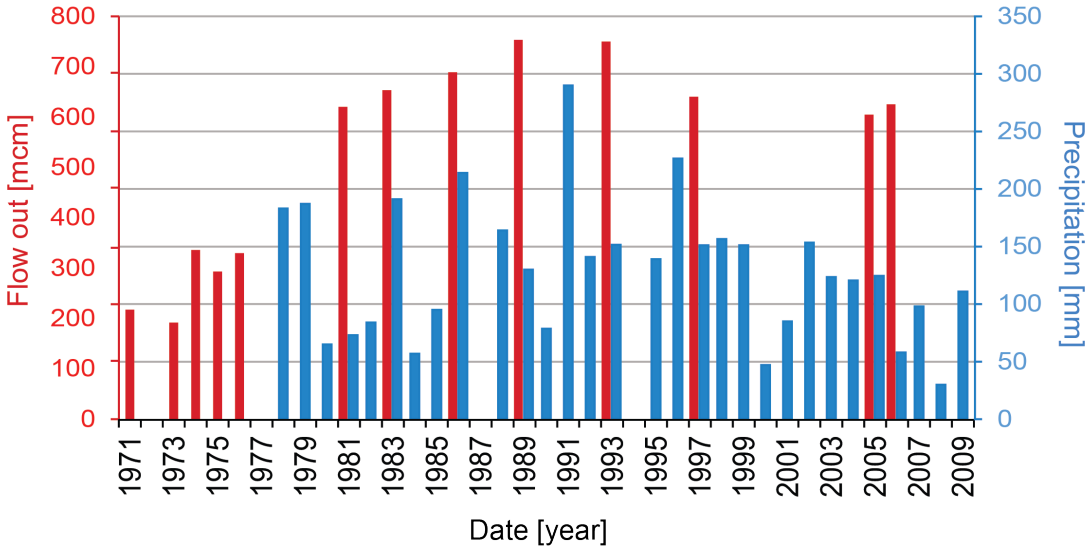

Figure 3: Precipitation (blue bars, right axis) and total well discharge (red bars, left axis) in different sampling years (Zayandehroodi, 2012). The precipitation data are extracted from the Davaran meteorology station (National code: 028-46), marked by a white triangle in Fig. 1.

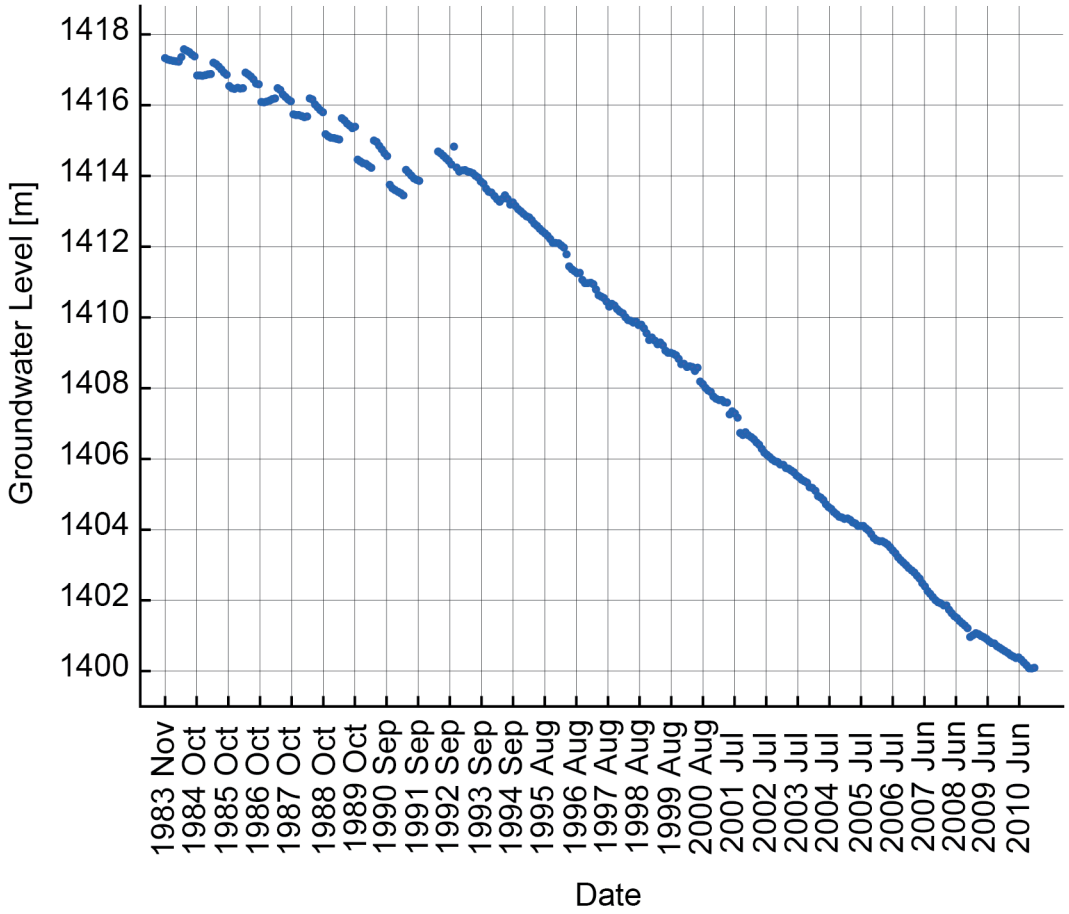

Figure 4: Average groundwater hydrograph of the Rafsanjan Plain from 1983 to 2010 (Zayandehroodi, 2012)

Groundwater is the main water supply source for irrigation activities in the region, and the total amount of groundwater extracted annually increased from approximately 200 million cubic metres (mcm) in the 1970s to more than 700 mcm in the late 1980s. The annual groundwater discharge in the region is estimated to be approximately 600 mcm/yr (Fig. 3), of which approximately 96% is consumed for agriculture. The region currently suffers from an approximately 200 mcm/yr deficit in the groundwater balance as a result of its agricultural and industrial water needs. The unrestrained exploitation of the aquifers has caused a significant groundwater level decline of approximately 17 m over the past 3 decades (Zayandehroodi, 2012), from 1417 m a.s.l. (above sea level) in 1983 to 1400 m a.s.l. in 2010 (Fig. 4). The number of deep wells drilled for irrigation

178 purposes has increased substantially in the past five decades, from approximately 70 in
179 the 1960s to more than 1300 in the 2000s (Jaghdani and Brummer, 2011), out of which
180 more than 600 wells tap water from a depth of 170-350 m (Fig. 5). The overexploitation
181 of groundwater resources leads to a reduction in pore pressure and results in
182 consolidation of the sedimentary layers as a consequence of groundwater level decline
183 (Terzaghi, 1925).

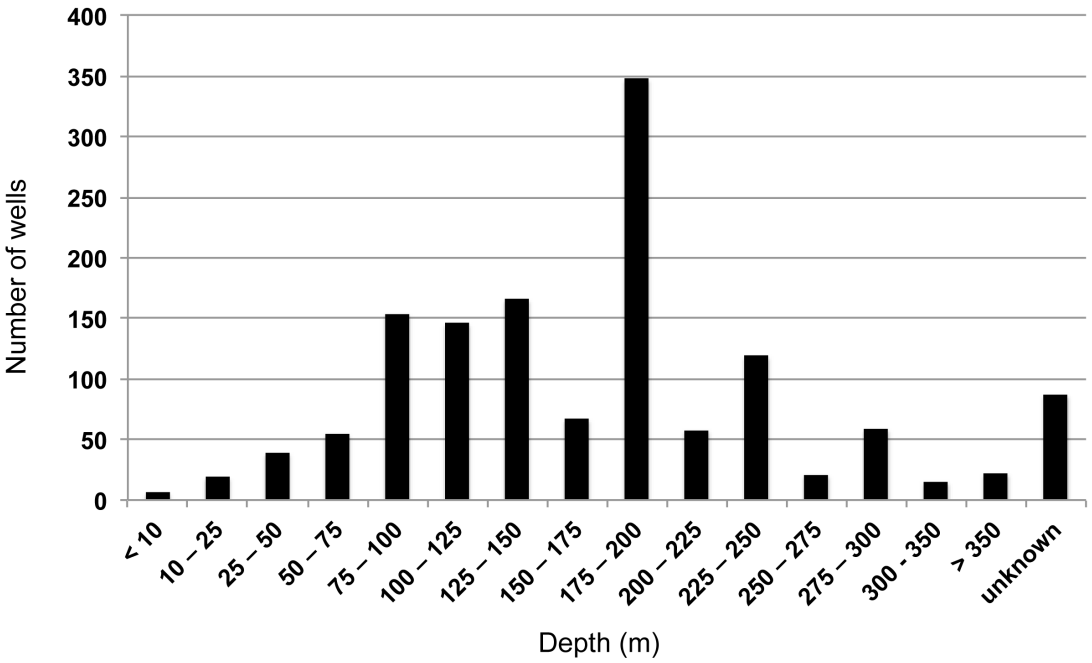

184

185 Figure 5: Distribution of depths to the water table in Rafsanjan. Modified after (Zayandehroodi, 2012)

186 **3. Method**

187 **3.1. InSAR analysis**

188 To derive the spatial and temporal changes in land subsidence in Rafsanjan, we utilized
189 5 sets of SAR images, including 16 Envisat ASAR images from a descending track
190 covering April 2003–May 2008, 23 Envisat ASAR images from an ascending track
191 covering June 2004–August 2007, 10 ALOS PALSAR images from an ascending track
192 covering September 2007–November 2010, and 32 S1 TOPS images, 16 from an

ascending track and 16 from a descending track, both covering the same time period between May 2015 and May 2016 (See Motagh et al. (2017) for the list of data). The outline of the SAR frames is shown in Figure 1. The mean incidence and heading angles of each SAR sensor are listed in Table 1.

Table 1: Geometric parameters of the different SAR sensors; des and asc stand for descending and ascending orbits

Sensor	Azimuth angle	Incidence angle
Envisat (des)	195°	23°
Envisat (asc)	344°	41°
ALOS (asc)	347°	39°
S1 (asc)	350°	37°
S1 (des)	190°	43°

We processed all the data using the SBAS time-series approach (Berardino et al., 2002). For the SBAS analysis, we first produced differential interferograms of the SAR data. The Envisat and ALOS interferograms were processed using the repeat-pass method implemented in the DORIS software (Kampes et al., 2003). The InSAR processing of the S1 interferometric wide-swath data was performed with GAMMA software (Wegmuller and Werner, 1997) using the spectral diversity method (Scheiber and Moreira, 2000) for precise coregistration of SAR data. Such a precise coregistration (offset estimation better than 0.001 for an azimuth resolution cell) is necessary for S1 interferometric processing to avoid azimuth phase variations in S1 interferograms caused by along-track differences in Doppler-centroids (Fattahi et al., 2016; Prats-Iraola et al., 2012). A 90-m digital elevation model that was derived from the NASA Shuttle Radar Topography Mission (SRTM) was used as the reference topography model for the topography-related phase correction and geocoding (Farr and Kobrick,

2000) of all the interferograms. Second, we performed a time-series analysis of differential interferograms using the StaMPS/MTI method (Hooper, 2008). For the Envisat and ALOS data, we first selected an initial set of candidates, the so-called Persistent Scatterer Candidate (PSC), using amplitude difference dispersion (Ferretti et al., 2001; Hooper, 2008):

$$D_A = \frac{\sigma_a}{\bar{a}}, \quad (1)$$

where σ_a stands for the standard deviation of the difference in amplitude between the master and slave, and $\bar{a}$ is the mean amplitude. A threshold value of 0.6 was used to select the initial sets of PSCs. The interferometric phase of the PSCs was then corrected for both spatially correlated contributions and spatially uncorrelated look angle errors to estimate phase noise through a measure called temporal coherency (γ_x), defined as (Hooper et al., 2004):

$$\gamma_x = \frac{1}{N}\left|\sum_{i=1}^{N} exp\left\{j\left(\psi_{x,i} - \widetilde{\psi}_{x,i} - \Delta\widehat{\psi}^{u}_{\theta,x,i}\right)\right\}\right|, \quad (2)$$

where $\psi_{x,i}$ is the wrapped phase of pixel x in the ith interferograms, $\tilde{\psi}_{x,i}$ is the estimate for the spatially correlated terms, $\hat{\psi}^{u}_{\theta,x,i}$ is the estimate of the spatially uncorrelated look angle error term, and N is the number of interferograms. The statistical analysis of the distribution derived from the temporal coherency in equation (2) leads to the selection of those pixels that exhibit slow decorrelation over short time intervals, which are the so-called slowly decorrelating filtered phase (SDFP) pixels. For the S1 interferograms, the SDFP pixels were selected using classical coherence thresholding (Berardino et al., 2003) because the Sentinel-1 satellite has a very stringent orbital control that ensures precise ground-track repeatability and small InSAR baselines on the order of 150 m (Geudtner et al., 2014; Yagüe-Martínez et al., 2016). Together with the short repeat

orbit cycle of 12 days, this results in a drastic improvement in the quality of small baseline S1 interferograms in comparison to C-band interferograms derived from data acquired by previous missions such as Envisat and ERS. Therefore, coherence thresholding enables the retrieval of a sufficient number of pixels that are suitable for deformation analysis. To reduce the computational cost, pixels exhibiting coherences greater than 0.5 in S1 interferograms were selected as SDFP pixels. Finally, the wrapped phase of the SDFP pixels was unwrapped using a 3-dimensional phase unwrapping approach (Hooper and Zebker, 2007), and a least-squares inversion was applied to retrieve the displacement time-series. The individual interferograms were checked for unwrapping errors and phase jumps in space, and those exhibiting large unwrapping errors were eliminated from the processing. The above procedure from SDFP pixel selection to least-squares inversion was then repeated until all interferograms were reliably unwrapped. Fig. 6 illustrates the spatial and temporal baselines for the final network of interferograms used for the time-series analysis. We constructed a total of 145 SBAS interferograms, including 8 from Envisat descending orbits, 41 from Envisat ascending orbits, 26 from ALOS, 34 from S1 ascending orbits and 36 from S1 descending orbits.

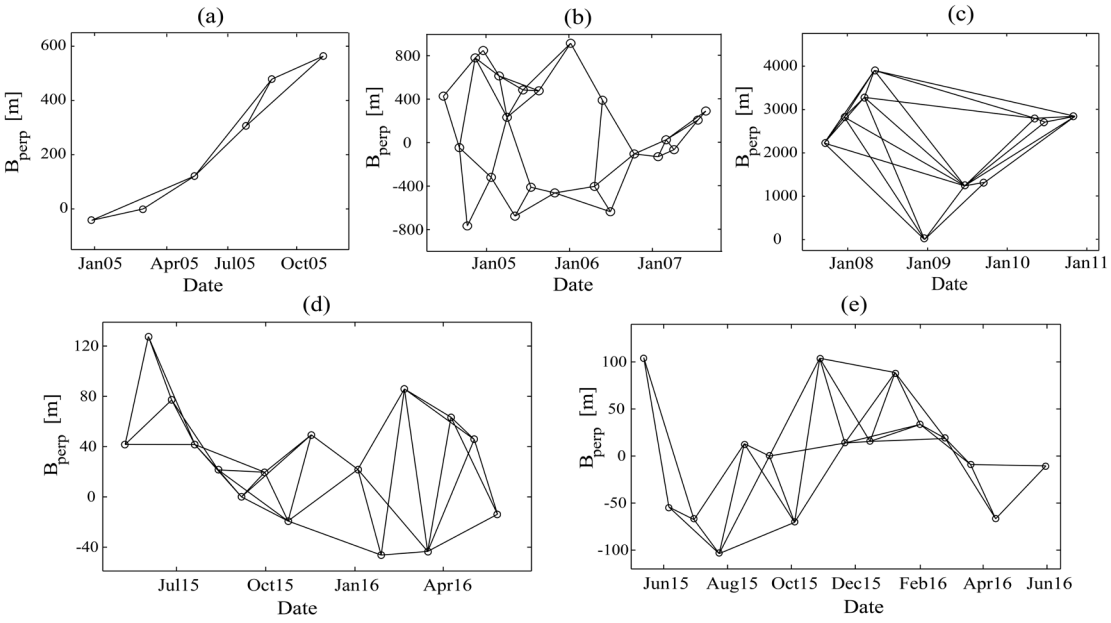

Figure 6. Plots of acquisition dates versus perpendicular baselines for the final network of the (a) Envisat descending, (b) Envisat ascending, (c) ALOS, (d) S1 ascending and (e) S1 descending data used for the time-series analysis. The circles represent SAR images, and the lines represent the small baseline interferograms.

3.2. Velocity decomposition

As indicated above, the 5 sets of InSAR observations used for assessing land subsidence in Rafsanjan represent data from different geometries (azimuth and incidence angles). For a single set of SAR data, the line-of-sight (LOS) velocity (V_{los}) that was derived for each pixel by applying the SBAS method can be expressed in the following way:

$$V_{los} = V_v \cos\theta - (V_e \cos\alpha - V_n \sin\alpha) \sin\theta, \quad (3)$$

where α is the azimuth of the LOS vector, θ is the incidence angle, and V_e, V_n, V_v are the velocities in the east–west, north–south and vertical directions, respectively. Due to the near polar orbits of spaceborne SAR systems, LOS measurements are least sensitive to displacements in the north-south direction. By excluding this component, equation (3) is transformed into the following form:

$$V_{los} = V_v \cos\theta - V_e \cos\alpha \sin\theta. \quad (4)$$

Equation (4) can be solved if for each pixel at least two independent measurements

from descending and ascending orbits exist to form the following matrix of equations:

$$\begin{pmatrix} V_{los}^{a} \\ V_{los}^{d} \end{pmatrix} = \begin{pmatrix} cos\theta^{a} & -cos\alpha^{a} sin\theta^{a} \\ cos\theta^{d} & -cos\alpha^{d} sin\theta^{d} \end{pmatrix} \begin{pmatrix} V_v \\ V_e \end{pmatrix}, \quad (5)$$

where the superscripts a and d refer to ascending and descending geometries, respectively. The SAR sensors used in this study cover different time periods, resulting in different temporal sampling of the ground motion. They also have different spatial resolutions that can affect the decomposition results (Samsonov and d'Oreye, 2012). We therefore applied equation (5) to the velocity maps retrieved from S1 data in ascending and descending orbits, which covered the same time period and have the same spatial resolution. The geocoded LOS displacement rates retrieved from S1 SBAS were first interpolated onto the same geographic grid points before inverting equation (5) to estimate the east-west and vertical displacement rates.

3.3. Compressibility and volume loss of the aquifer

Groundwater level measurements carried out in wells are of key importance for the interpretation of surface deformation in developed ground water basins (Hoffmann et al., 2003; Lu and Danskin, 2001; Tomás et al., 2010b). The storage coefficient or storativity (S) is one of the main hydraulic parameters and can be used for a better understanding of reservoir properties and deformability characteristics of an aquifer system (Riley, 1969). It is defined as the volume of water of an aquifer released from or taken into storage V_w per unit area A per unit change in the hydraulic head h (Bundschuh, 2010):

$$S = \frac{d}{dh}\left(\frac{V_w}{A}\right). \quad (6)$$

Unconfined aquifers that release large amounts of water by draining the pores of the aquifer have typical storativity values of 0.05-0.3, whereas confined aquifers have very low storativity values of less than 0.01 and as little as 10^{-5}.

To estimate the storage coefficients, we used the relationship between head change measurements and surface deformation (Calderhead et al., 2011):

$$\delta = \Delta h \times S_k, \quad (7)$$

where δ is subsidence, Δh is the fluctuation in the hydraulic head, and S_k represents the sum of the skeletal storage coefficients (dimensionless) of both aquifers and aquitards (Galloway and Hoffmann, 2007). S_k was expressed in the following way (Ezquerro et al., 2014):

$$S_k = (S_{sk} + S_{sw}) \times D, \quad (8)$$

where D is the thickness of the aquifer system, S_{sk} is the skeletal specific storage (m^{-1}) or storativity per unit aquifer thickness, and S_{sw} is the water specific storage, which is defined as (Ezquerro et al., 2014):

$$S_{sw} = (n \times \gamma)/E_w. \quad (9)$$

In equation (9), n is the porosity of the aquifer, γ is the unit weight of water, and E_w is the bulk modulus of elasticity of water. For a compacting aquifer system such as that in Rafsanjan, $S_{sk} >> S_w$. Two separate parameters of elastic skeletal specific storage (S_{ske}) and inelastic skeletal specific storage (S_{skv}) are often used to separate elastic and recoverable deformation from inelastic and non-recoverable deformation (Galloway and Hoffmann, 2007; Hung et al., 2012):

$$S_{sk} = \begin{cases} S_{ske}, & for\ h < h_p \\ S_{skv}, & for\ h > h_p' \end{cases} \quad (10)$$

where h_p in equation (10) represents the preconsolidation head, which is the lowest hydraulic head experienced by the material, and h represents the position of the hydraulic head.

In this work, the skeletal storage coefficient was computed using piezometric series at 15 wells for which we have information on water tables for the period 2004-2010. To

determine the associated temporal evolution of the ground surface displacement at each well, average displacement time-series of all coherent pixels within 300 m of a well were computed. Because Envisat ascending, which covered 2004-2007, and ALOS, which covered 2007-2010, have similar acquisition geometries, their vertical displacement time-series results were first obtained by converting the LOS displacements to the vertical direction by ignoring the horizontal displacement. The two series were then merged by estimating the vertical offsets between two separated time-series resulting from the assumed linear velocity change. We then assessed the correlation between the time-series of groundwater level and the surface subsidence around each well. For those wells showing a positive correlation, we linearly interpolated the time series of both InSAR and water levels to the monthly interval and calculated the slope of the groundwater level change versus displacement data to determine the storage coefficient.

Having estimated the aquifer storage coefficients, we could also calculate the storage volume changes of the aquifer, ΔV, as

$$\Delta V = A \times \Delta h \times \bar{S}, \tag{11}$$

in which $\bar{S}$ represents the mean storage coefficient of the entire aquifer, A is the areal extent of the aquifer, and Δh is the variation in the stress state, which can be expressed as a piezometric level fall.

4. Results and Discussion

4.1. InSAR time-series results

Fig. 7 illustrates maps of the average annual displacement rates along the satellite LOS directions derived from SBAS processing of Envisat (Figs. 7a-b), ALOS (Fig. 7c) and S1 (Figs. 7d-e) SAR data (See Motagh et al. (2017) for data access). The velocity maps

were generated with respect to a reference point that was selected in an area where levelling observations between 1997 and 2006 showed no subsidence (Fig. 7). The observation periods for the velocity maps are shown in Fig. 7f. The results in Fig. 7 suggest that an area of approximately 1000 km^2 of the plain was adversely affected by a surface subsidence that exceeded 5 cm/year. The maximum LOS velocity obtained by the different sensors exceeded 20 cm/yr of subsidence.

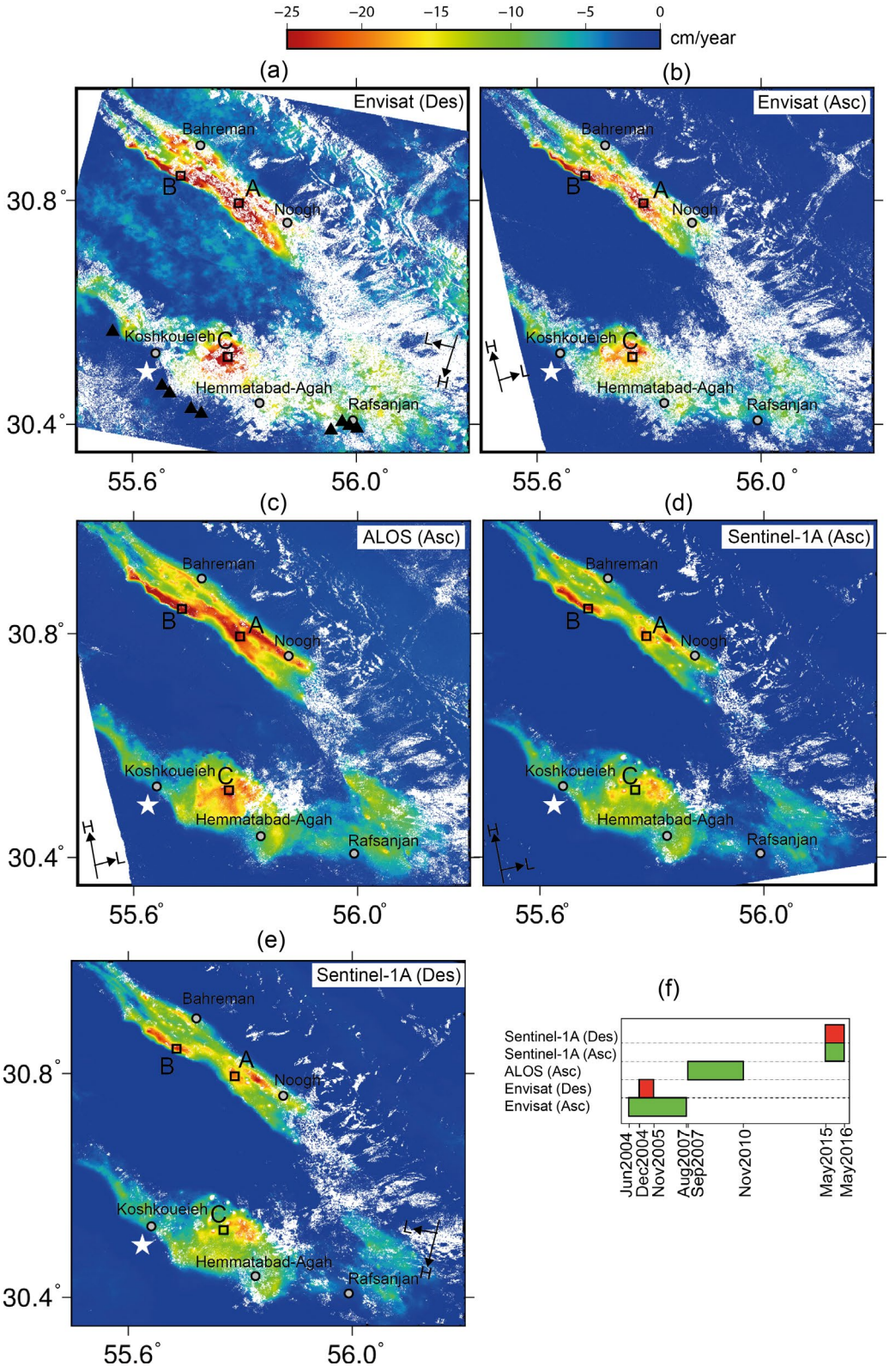

Figure 7: Average LOS velocity maps derived from (a) Envisat descending, (b) Envisat ascending, (c) ALOS (d) S1 ascending, and (e) S1 descending (See Motagh et al. (2017) for data access); the observation periods corresponding to the velocity maps are shown in (f). The white stars indicate the location of the reference point used in the SBAS-processing. For the points labelled A, B, and C, the

displacement time-series are shown in Fig. 8. The vectors H and L represent the satellite heading and look angle. The grey-filled circles show the main townships and villages.

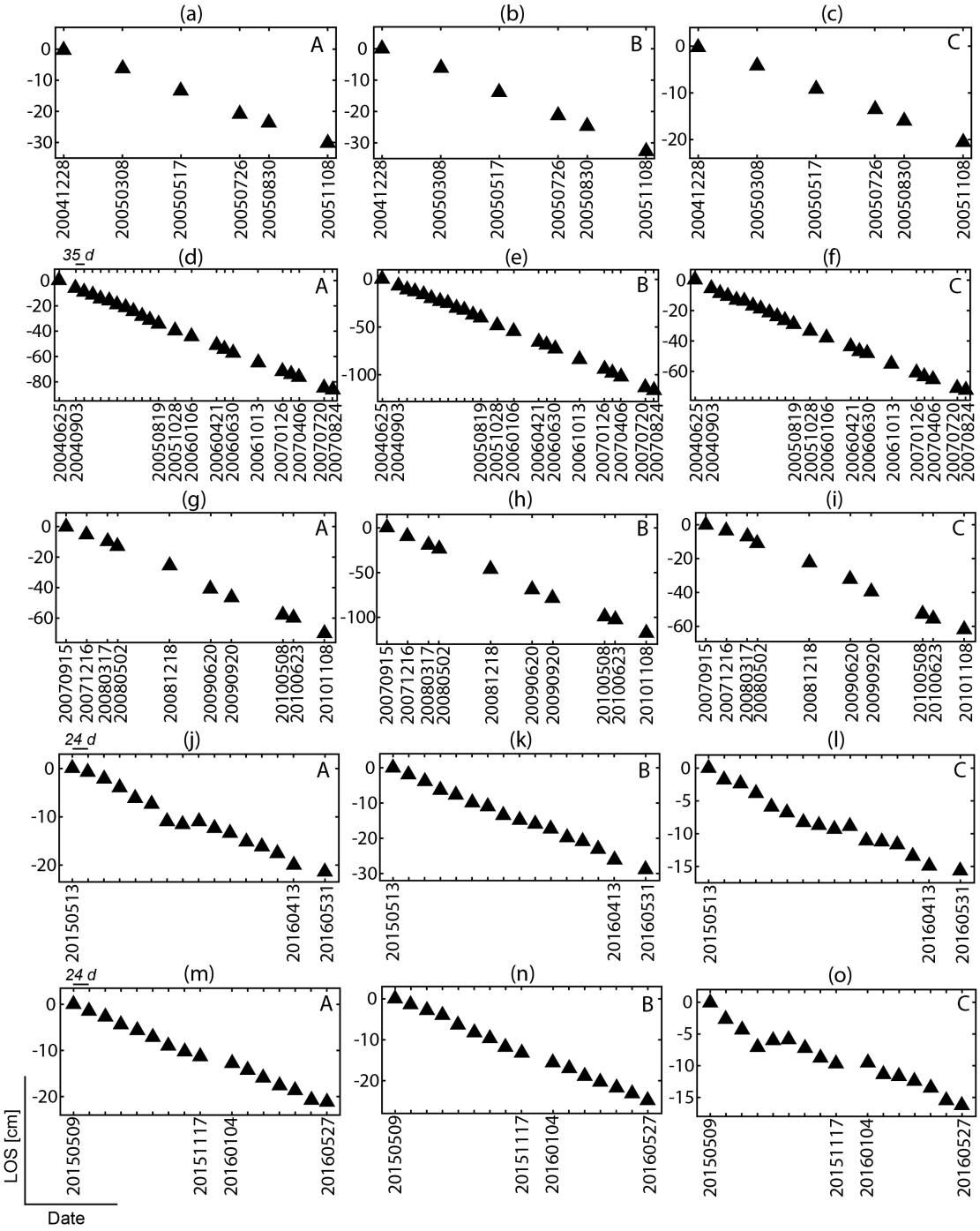

Figure 8: Displacement time series at the locations of points A, B, and C (Fig. 7) are shown in (a,b,c), (d,e,f), (g,h,i), (j,k,l), and (m,n,o), which correspond to Envisat descending, Envisat ascending ALOS, S1 ascending and S1 descending, respectively.

Comparison of the velocity maps in Fig. 7 indicates that the spatial patterns of the areas

affected by subsidence were similar between the different sensors. We can delineate at least 3 spatially significant subsidence zones where large LOS rates (<=-20 cm/yr) were observed in all the velocity maps: two subsidence bowls in the Noogh-Bahreman valley (Points A and B in Fig. 7) and one subsidence bowl in the Koshkoueieh-Rafsanjan area (Point C in Fig. 7). There was also a conspicuous region north of Rafsanjan city that showed subsidence, albeit at a lesser rate compared to the main anomalies discussed above.

Table 2: Maximum cumulative LOS displacements at points A, B and C (Figs. 7-8) retrieved from different sensors. The numbers in parentheses correspond to the average linear velocities for the time period covered by each sensor.

Sensor	A	B	C
Envisat (des) Dec2004-Nov2005	-31.75 (-37.5 cm/yr)	-34.85 (-41.25 cm/yr)	-22.15 (-26.14 cm/yr)
Envisat (asc) Jun2004-Aug2007	-82.6 (-25.9 cm/yr)	-112.67 (-35.74 cm/yr)	-68.72 (-21.52 cm/yr)
ALOS (asc) Sep2007-Nov2010	-71.12 (-23.62 cm/yr)	-118.64 (-38.96 cm/yr)	-63.47 (-20.82 cm/yr)
S1 (asc) May2015-May2016	-19.49 (-20 cm/yr)	-26.85 (-25.54 cm/yr)	-13.74 (-13.95 cm/yr)
S1 (des) May2015-May2016	-19.05 (-19.72 cm/yr)	-22.65 (-22.66 cm/yr)	-14.09 (-14.06 cm/yr)

Due to their relatively steep incidence angles (Table 1), all the SAR sensors used in this study are most sensitive to vertical displacement, whereas east-west motions will appear differently in the ascending and descending time-series and velocity maps. Fig. 8 illustrates temporal patterns of LOS displacement for points A, B and C in the main subsidence areas of Noogh-Bahreman and Koshkoueieh-Rafsanjan. As illustrated in Fig. 8, the LOS displacements at our selected points were almost linear in time, in

366 particular for the period 2004-2010 analysed using the Envisat and ALOS data. A
367 similar linear trend is also visible in the S1 displacement time-series (Figs. 8j-o).
368 However, the higher temporal resolution of the S1 data allowed the progression of
369 subsidence to be monitored in much more detail compared to other sensors. For
370 example, at both points A and B we observed a deceleration appearing in the LOS
371 displacement rate between May and June 2015, which was followed by a period of
372 more rapid subsidence. Such temporal changes could not be resolved in the Envisat or
373 ALOS displacement time-series due to their lower temporal resolutions.

374 Although the areas affected by land subsidence as detected by the different sensors in
375 Fig. 7 were similar, the rate of subsidence was lower during the period of S1 data
376 coverage compared to the previous epochs covered by Envisat and ALOS. This can
377 also be inferred by comparing the average linear velocities at points A, B and C that
378 were derived from the ALOS, Envisat ascending and S1 ascending data listed in Table
379 2; ALOS, Envisat ascending and S1 ascending have similar acquisition geometries
380 (Table 1) and therefore comparable sensitivities to ground surface deformation. For
381 example, the rate of subsidence at point A decreased from ~ -26 cm/yr during June
382 2004-August 2007, to -24 cm/yr during September 2007-November 2010 and further
383 to -20 cm/yr during May 2015-May 2016. Similarly, the 2015-2016 S1-derived
384 subsidence rates at points B and C showed reductions of up to 37% and 33%,
385 respectively, in comparison to the displacement rate inferred during the 2000s by
386 Envisat and ALOS.

387 **4.2. Horizontal and vertical displacement rates and field check**

388 The average vertical and horizontal displacement rates that were derived from the
389 decomposition of the S1 ascending and descending LOS velocities for Noogh-

Bahreman and Koshkoueieh-Rafsanjan are shown in Figures 9 and 10, respectively; the colour coding depicts the vertical subsidence rates, and the arrows show the horizontal displacement rates. For visualization purposes, only one percent of the vectors with horizontal displacement rates greater than 2 cm/yr were randomly selected and plotted in those figures. The maximum vertical subsidence rate in the agricultural regions of the Rafsanjan plain amounted to 30 cm/yr for the period between May 2015 and May 2016. The largest horizontal displacement rates were observed mainly on the margins of the subsidence areas, where they amounted to 3-5 cm/yr. The magnitude of the horizontal displacement decreased towards the subsidence centre.

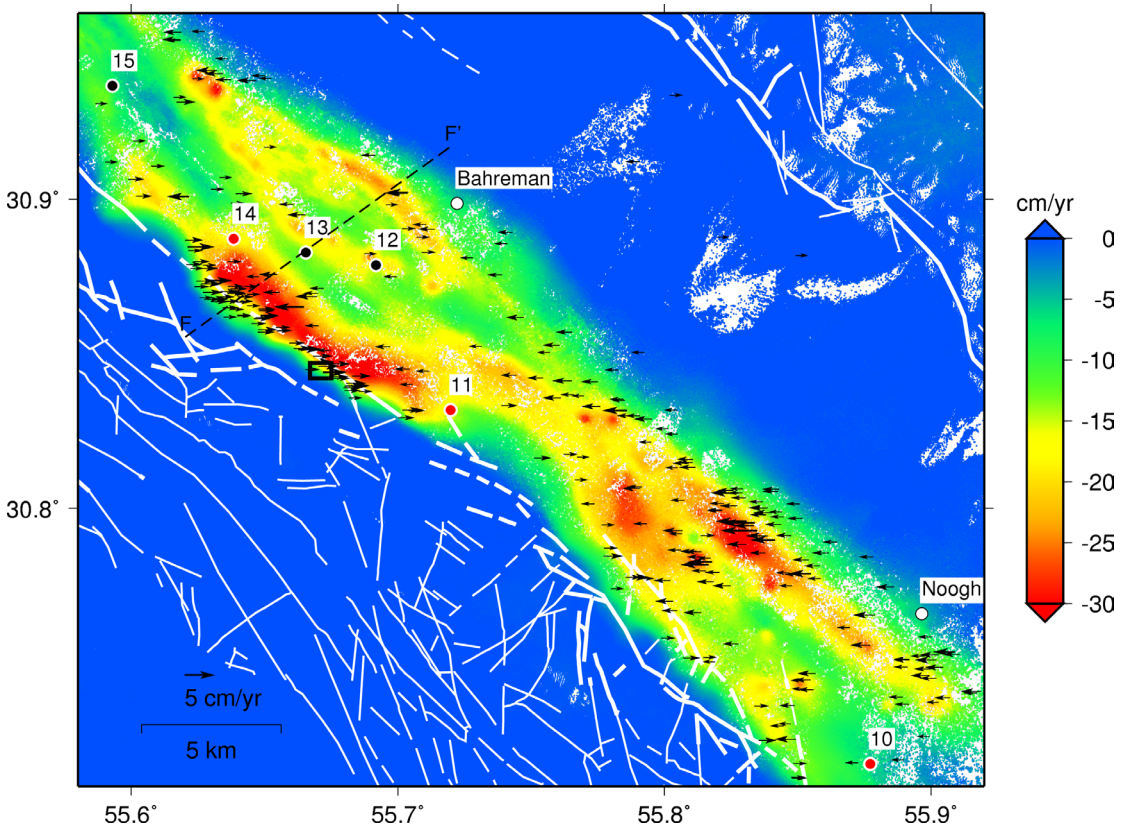

Figure 9: Average 2015-2016 vertical and east-west displacement rates in Noogh-Bahreman derived from the decomposition of the S1 ascending and descending LOS velocities; The background color corresponds to vertical displacement rates and arrows to horizontal displacement rates. The black and red-filled circles correspond to the locations of selected piezometric wells, and the well numbers refer to the well records plotted in Figs. 16-17. The red-filled circles mark the locations of the wells with negative

correlations between ground surface displacement and groundwater level (see Fig. 16). The white lines depict the faults and lineaments also shown in Fig. 2. The locations of the field pictures shown in Fig. 12 are labelled by the black square. FF' indicates the location of the profile analysed in Fig. 11. The white-filled circles show the main townships and villages.

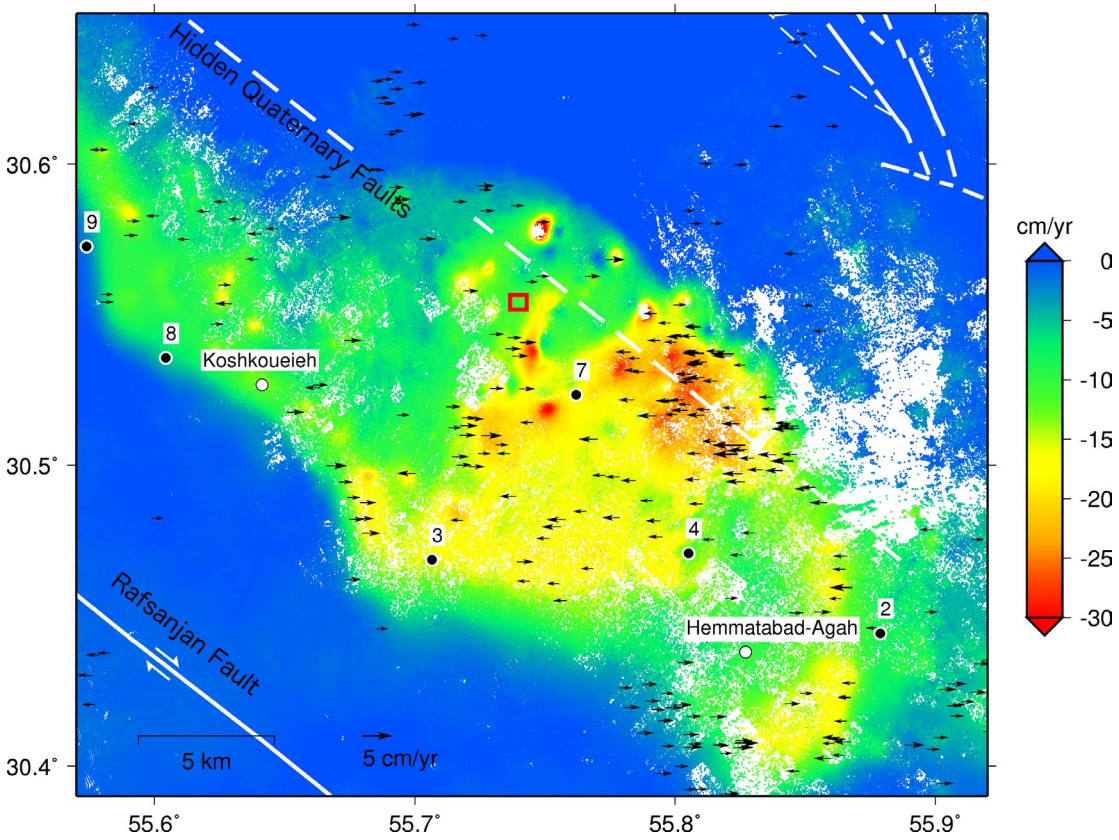

Figure 10: Average 2015-2016 vertical and east-west displacement rates in Koshkoueieh-Rafsanjan derived from the decomposition of the S1 ascending and descending LOS velocities; The background color corresponds to vertical displacement rates and arrows to horizontal displacement rates. The black-filled circles correspond to the locations of selected piezometric wells, and the well numbers refer to the well records plotted in Figs. 16-17. The white lines depict the faults and lineaments also shown in Fig. 2. The locations of the field pictures shown in Fig. 13 are labelled by the red square. The white-filled circles show the main townships and villages.

To investigate the differences between the vertical and horizontal displacement rates more quantitatively, we extracted a profile crossing one of the main large-scale subsidence bowls in Nogh-Bahreman (FF' in Fig. 9). Figure 11 depicts the

displacement rates in the horizontal and vertical directions along that profile. The horizontal rates were zero in the areas where the vertical gradients were zero (relative maximums and minimums in the vertical profile at 3.1, 4.9, 6.3, 7 and 9 km, marked with the grey lines in Fig. 11). The profile also indicates that the maximum horizontal rates occurred in the area with the maximum vertical gradient.

In each subsidence bowl, we observed eastward motion west of the subsidence centre and westward motion east of the centre. In other words, there was movement towards the subsidence centre (Samieie-Esfahany et al., 2009). These results also indicate that the largest horizontal displacement along the profile amounted to approximately one-tenth of the maximum subsidence.

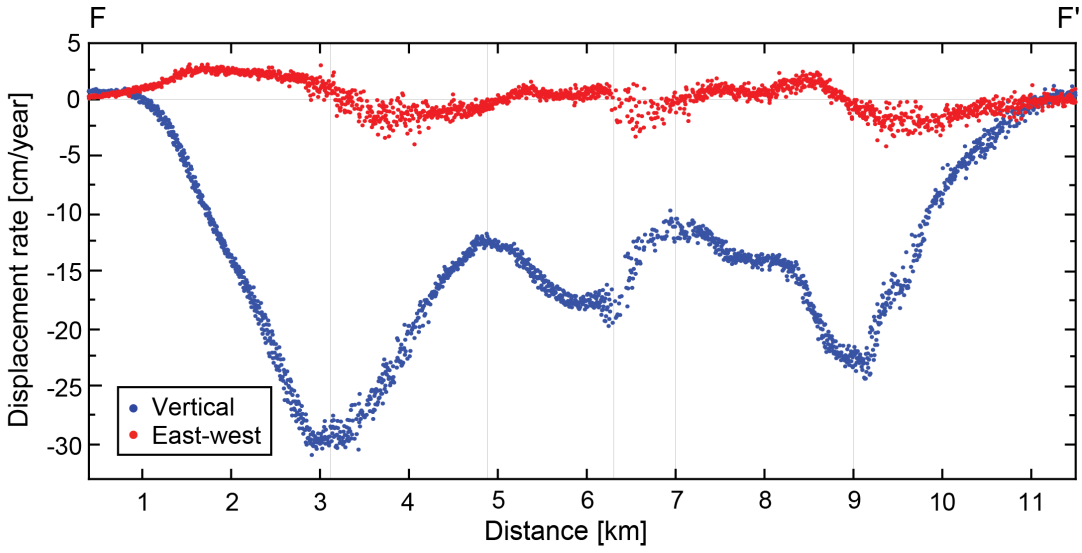

Figure 11: Vertical and horizontal displacement rates along the FF' shown in Fig. 9. The positive values in the east-west profile correspond to eastward motion and negative values to westward motion.

As shown in Fig. 9, one of the main subsidence bowls in Noogh-Bahreman is closely bordered along its southern margin by the Quaternary Bahreman fault, exhibiting a large displacement gradient of 30 cm along a distance of < 1.5 km. In our field survey in June 2015, we found many wide fissures and tension cracks that have recently

438 developed in response to the basin subsidence and differential deformation across the
439 fault. In Fig. 12, a 200-300 m wide crack zone is depicted on a Google Earth image,
440 with the overlaid coloured points showing the vertical displacement rates. Field photos
441 of the crack zone are shown in Figs. 12b-f. The orientation of the tension cracks
442 identified in the Noogh-Bahreman valley mainly follows the orientation of the
443 Quaternary faults that bound the subsidence area in this region and separate it from the
444 adjacent saddle structure in the south. The saddle structure is stable, but the valley
445 alluvium is subsiding, causing the formation of shallow en-echelon cracks due to
446 differential compaction of the Rafsanjan aquifer across the fault. In some cases, the
447 cracks intersect with newly developed shallow gullies, as indicated by the black arrows
448 in Figs. 12d-f.

449 Our field surveys have also shown that this is not a localized phenomenon. We also
450 observed several recent compaction-related earth fissures with depths of up to 3-4 m in
451 the southern valley of Koshkoueieh-Rafsanjan (the red square in Fig. 10). These earth
452 fissures are marked on the Google Earth image shown in Fig. 13 accompanied by the
453 field pictures (Figs. 13b-d). In contrast to the Noogh-Bahreman valley, the cracks
454 observed in the Koshkoueieh-Rafsanjan valley do not always run parallel to each other
455 and/or to the strike of the faults. They have larger depths and exhibit clear evidence of
456 vertical displacement formed in fine-grained alluvial-fan deposits. In both regions -
457 Noogh-Bahreman and Koshkoueieh-Rafsanjan - the areas of exposed bedrock
458 separated from the basin sediments by the Quaternary faults do not show any signs of
459 crack formation, excluding the reactivation of pre-existing faults as the source of the
460 observed cracks. Therefore, we conclude that the formation of these en-echelon,
461 multiple parallel, and branching fissures (Figs. 12 and 13) indicate inelastic
462 deformation resulting from differential compaction in the alluvial basin, which has

undergone significant groundwater depletion (Conway, 2015; Holzer and Pampeyan, 1981).

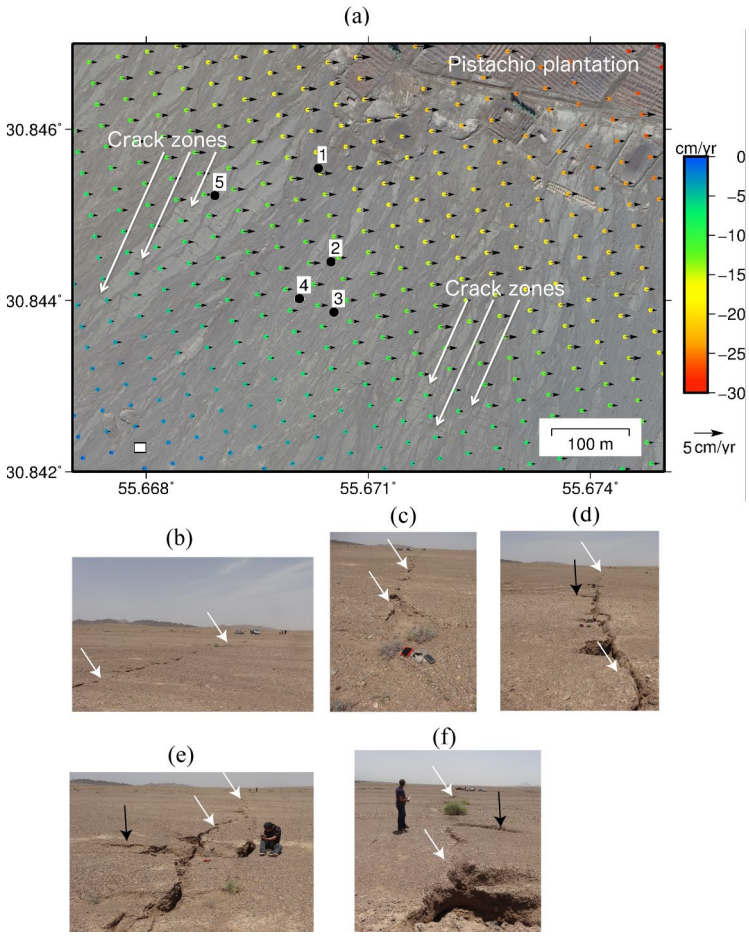

Figure 12: (a) The color-coded points show the vertical displacement rates derived from the decomposition of the S1 ascending and descending LOS velocities. They are overlain on the Google-earth image of the area depicted by the black square in Fig. 9. The black vectors stand for horizontal displacement. The horizontal vectors are shown with respect to the point marked by a white square to illustrate local horizontal gradient in the region. (b), (c), (d), (e) and (f) are field photographs of the areas labelled 1, 2, 3, 4, and 5, respectively, and marked with black dots in Fig. 12a.

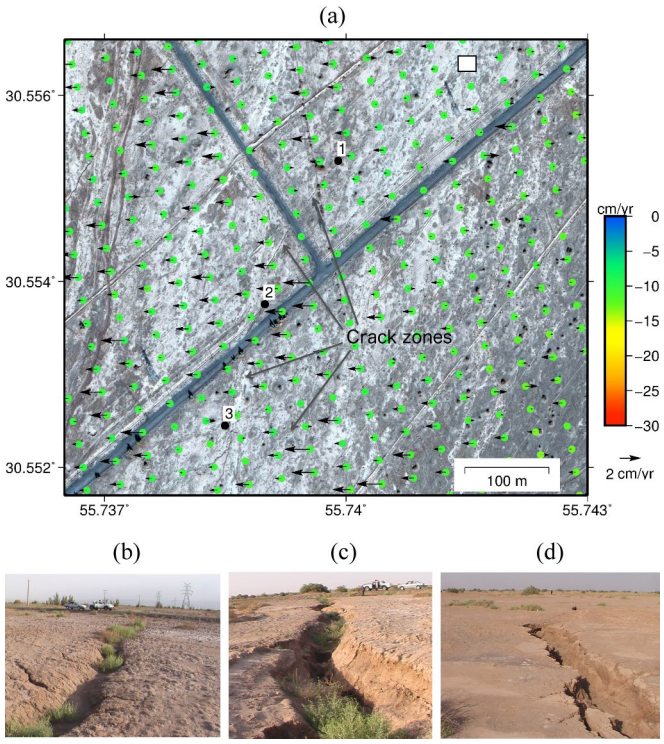

Figure 13: (a) The colour-coded points show the vertical displacement rates derived from the decomposition of the S1 ascending and descending LOS velocities. They are overlain on a Google-earth image of the area depicted by the red square in Fig. 10. The black vectors represent horizontal displacement. These horizontal vectors are shown with respect to the point marked by a white square to illustrate the local horizontal gradient in the region. (b), (c), and (d) are field photographs of the areas labelled 1, 2, and 3, respectively, and marked with black dots in Fig. 13a.

4.3. Accuracy and consistency assessment

The InSAR results from the different datasets were compared to assess their interconsistency. Because of the different densities and locations of the displacement points, the results from the different datasets were first resampled onto a grid with a 100 m spacing. To compensate for the effect of the differing incidence angles, the results were then converted from the LOS to vertical direction, assuming the only component of displacement was vertical. Fig. 14 shows scatter plots of the subsidence rates derived from the different datasets, whereas the S1 ascending results were chosen as the reference for comparison. All the results are in general agreement with each

other. A high correlation coefficient of 0.8 was observed, indicating the general reliability of the measurements. The best correlation was between the ascending and descending S1 results. This is because the two S1 datasets covered almost the same time period, whereas the data acquisition was only offset by a 4-day difference. Therefore, that sensor can provide similar temporal sampling of the subsidence rates, which resulted in the strong 97% correlation. The weaker correlation observed between S1 ascending and the other sensors was partly caused by changes in the subsidence rates during the different time intervals and partly by the slight differences in the incidence and heading angles between the different sensors.

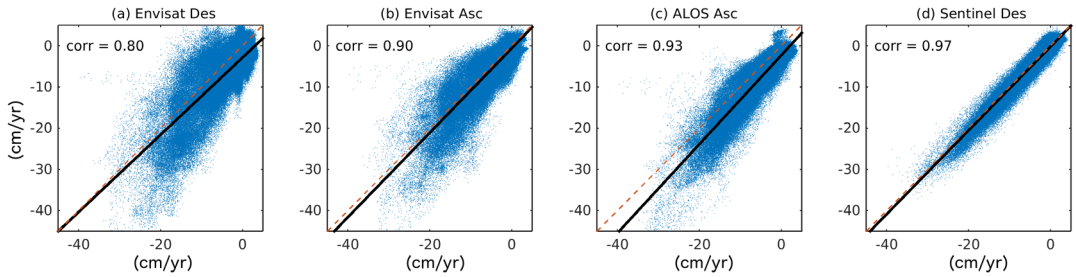

Figure 14: Correlation analysis for vertical displacement rates derived from S1 ascending and (a) Envisat descending, (b) Envisat ascending, (c) ALOS ascending, and (d) S1 descending. Overall correlation coefficients are indicated in each scatter plot. The dashed line marks identical vertical displacement rates, and the black bold line shows the linear trend.

Accuracy assessments of InSAR results need to be based on independent measurements in the same area and during the same time period covered by InSAR. However, subsidence measurements in Rafsanjan plain are scarce, except for some levelling measurements conducted between 1997 and 2006 by the National Cartographic Centre (NCC) of Iran along a 180-km profile. The levelling line included 50 measurement points, but only 9 of them, which covered a distance of 45 km, fell within the area covered by the InSAR analysis.

For comparison, InSAR displacement rates were extracted inside a 100-m buffer zone perpendicular to the levelling line. Furthermore, the LOS InSAR displacement rates were converted to vertical displacement to enable a comparison with the levelling results. As illustrated in Fig. 15, the levelling and different InSAR measurements showed general agreement at the levelling points. It is worth noting that although the levelling points along the first 20 km of the profile were apparently stable, the InSAR results revealed a significant subsidence area at 3 km. This subsidence is not observable in the levelling because of the large spacing of the levelling points along the profile. There was also another significant subsidence centre at 32 km, which was not adequately covered by the levelling profile due to its poor spatial sampling.

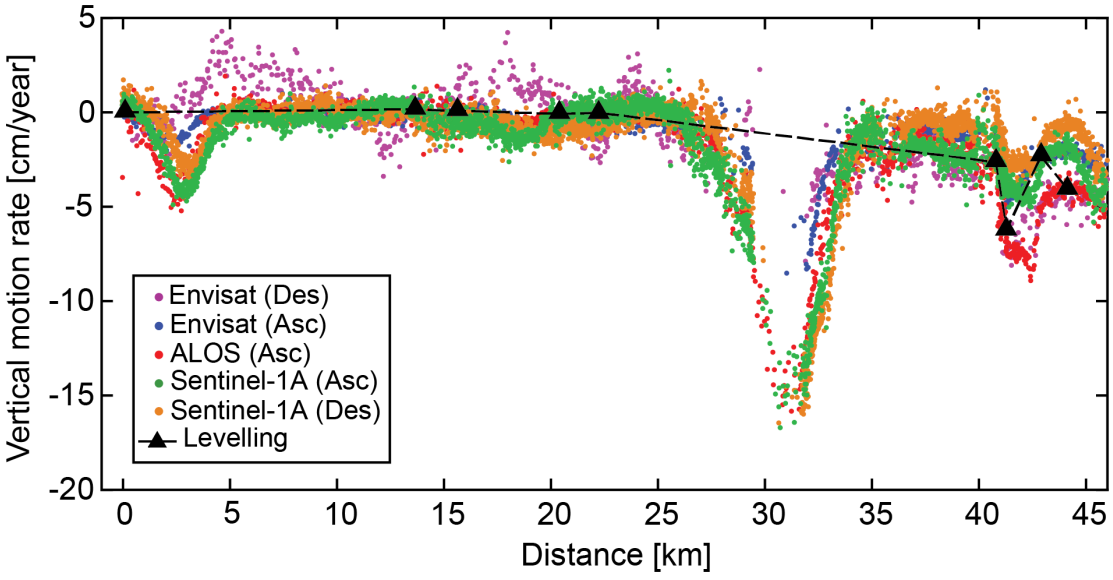

Figure 15: Subsidence rates derived from levelling and InSAR measurements along the levelling points indicated by triangles in Fig. 7a. The purple, blue, red, green, and orange points correspond to the Envisat descending track, Envisat ascending, ALOS, S1 ascending, and S1 descending results. The black triangles show the levelling results.

Table 3 lists the differences and the root-mean-square errors (RMSE) of the differences in subsidence rates at the levelling points derived from the levelling surveys and InSAR measurements. The InSAR points within a radius of 100-m around each levelling point

were averaged for comparison with the levelling data. The average RMSE values at all the levelling points were 12, 9, 8, 12 and 19 mm/yr, which correspond to Envisat descending, Envisat ascending, ALOS, S1 ascending and S1 descending, respectively. Table 3 shows that the minimum RMSE occurred at points in which the subsidence rates were the smallest, whereas the maximum RMSE occurred in the last three points characterized by the highest subsidence rates and variability over time. Excluding the last three points from the analysis resulted in a reduction in the RMSE values to 5, 7, 3, 7, and 10 mm/yr for Envisat descending, Envisat ascending, ALOS, S1 ascending and S1 descending, respectively.

The difference values listed in Table 3 might have been caused by either the effect of the horizontal displacement or the different time intervals of the different measurements. The locations of the levelling points are close to the subsidence margin (Fig. 7a), where horizontal displacement can influence the LOS result. Therefore, converting the LOS results to vertical displacement by ignoring the horizontal component might have contributed to the difference between the levelling and InSAR measurements. For a further analysis of this effect, we computed the differences in the vertical displacement rates between the levelling survey and the ones derived by the decomposition of the S1 data in the ascending and descending orbits (Fig. 10). However, the result of this comparison showed that there were no significant improvements in the difference and RMSE values (last column in Table 3). Therefore, it is more likely that the different time intervals of the measurements direct influenced the RMSE values listed in Table 3.

Table 3: Differences between the InSAR-derived vertical displacement rates and levelling results for points 1 to 9. The InSAR results were averaged within a radius of

552 100 m around each levelling point. The last row indicates the average RMSEs for all
553 points related to each sensor. The units are in mm/yr.

	Envisat (Des)	Envisat (Asc)	ALOS (Asc)	S1 (Asc)	S1 (Des)	Vertical*
1	4.33	2.00	-6.47	7.37	10.35	4.84
2	3.82	0.82	-0.10	2.06	-2.57	-2.41
3	11.26	-0.01	-3.74	-4.63	-3.43	-7.58
4	5.20	-1.80	1.30	0.05	-7.59	-7.54
5	-14.17	-0.61	2.31	3.24	-4.60	-3.64
6	-2.53	2.90	11.10	9.66	23.78	11.51
7	-11.67	15.79	7.27	23.66	35.60	25.46
8	-27.58	1.38	-12.98	-4.75	6.28	-3.01
9	-3.84	21.63	13.36	24.01	35.73	25.61
RMSE	12.05	9.04	8.07	12.22	19.30	13.34

554 * The values in this column were computed from decomposition result (Fig. 10)

555 **4.4. Correlation between subsidence and head decline**

556 Fig. 16 illustrates the time-series of the vertical displacement versus changes in the
557 groundwater level records at 15 piezometric wells (for the location, see Figs. 9-10). In
558 most of the cases, the trends in the InSAR time-series displacement and groundwater
559 level variation were similar, resulting in a positive correlation between subsidence and
560 a decline in groundwater level of more than 85%. However, there were some wells,
561 namely piezometers 10, 11, and 14, which are marked by red-filled circles in Fig. 9, for
562 which we observed a negative correlation between groundwater level change and
563 surface deformation. The water rise in these wells may indicate local differences in
564 groundwater extraction or may have been due to a recent ban on pumping in the region
565 undertaken by local authorities (Zayandehroodi, 2012). The high correlations between
566 the subsidence and decreasing groundwater levels in most of the piezometric wells

567 suggests that subsidence in the Rafsanjan basin is of anthropogenic origin (Bell et al.,
568 2002; Galloway and Burbey, 2011) as a result of human-induced compaction due to
569 massive pumping within the upper 300 m (Fig. 4) of the unconsolidated sediments
570 hosting the aquifer system.
571 Pumping-induced subsidence in a basin fill aquifer results mainly from the irreversible
572 compaction of fine-grained silt and clay layers (aquitard) during a prolonged drainage
573 process and from the minor elastic compaction of coarse-grained conglomerate and
574 sand deposits in the aquifer (Chen et al., 2007). As shown in Fig. 16, the water table
575 curve in most of the wells is dominated by a clear declining trend, with only small
576 seasonal components and no signs of major recovery. A comparable situation is seen in
577 the InSAR results: a dominant declining trend with no significant seasonal fluctuations.
578 These results suggest that a quasi-inelastic compaction dominates the deformation
579 regime in the Rafsanjan basin, which in turn also progresses up to the surface, where it
580 expresses itself by cracks and earth fissures such as those shown in Figs. 12-13.
581 According to the monitoring records, the ground level continues to show subsidence
582 for wells 10, 11 and 14, in which groundwater table began to rise again in 2004. This
583 indicates that any potential elastic rebound and uplift due to groundwater recovery at
584 those localities has been unable to overcome the residual compression of the aquifer
585 and the aquitard caused by past piezometric drawdown. The high-rate of subsidence in
586 the Rafsanjan basin, at some locations exceeding 20 cm/yr, cannot be attributed to the
587 natural soil compaction or tectonic loading because their estimated rates are generally
588 expected to be < 1 cm/yr (Chen et al., 2007; Kim et al., 2015).

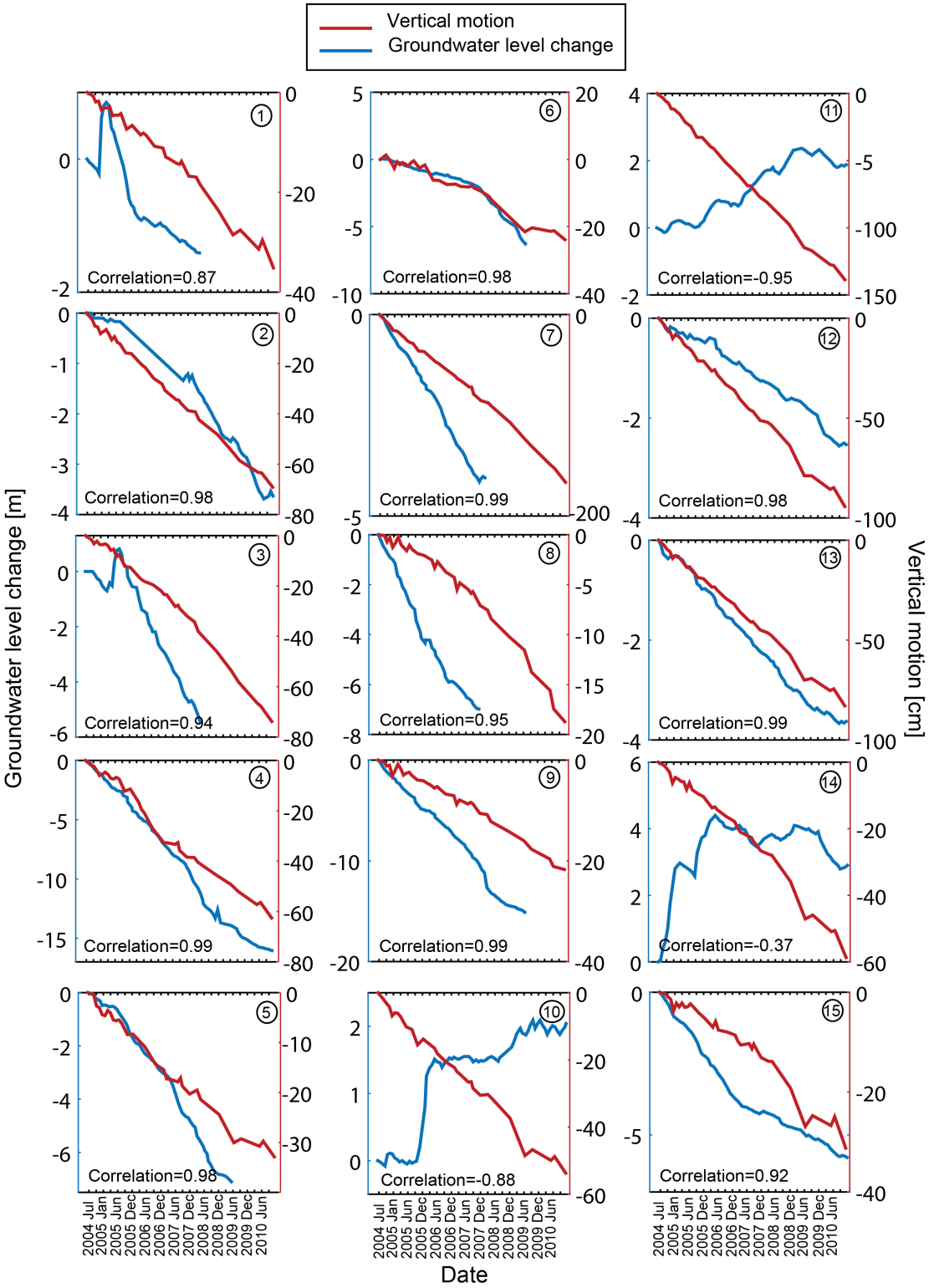

589

590 Figure 16: Correlations between the InSAR and groundwater level measurements at selected piezometric
591 wells. For the location and number of wells, refer to Figs. 9-10. The blue curves and left y-axes
592 correspond to head levels, and the red curves and the right y-axes correspond to SBAS-derived
593 displacement rates.

4.5. Storage coefficients and volume-storage loss

Fig. 17 illustrates the estimated storage coefficients obtained by analysing the relationship between the InSAR displacement time-series and contemporaneous measurements of water level at the piezometric wells. The estimated coefficients vary greatly, from 8.0×10^{-3} at the borders of the subsidence zones (piezometer 8) to 0.37 (e.g., piezometer 12) in the centre (Figs. 9-10). This is due to the variable relationship between applied stress (head change) and strain (displacement), which is observed even in the same area. For example, borehole 15 in Noogh-Bahreman valley showed 30 cm of subsidence for a piezometric decline of 5-6 m (Fig. 16), whereas boreholes 12 and 13 showed greater subsidences (up to 100 cm) for a lesser piezometric drop of 2-3 m. The estimated coefficients varied from 0.05 (borehole 15) at the margin of the main subsidence bowl to 0.37 (borehole 12) in the centre. The same pattern was observed in the Koshkoueieh-Rafsanjan valley; a moderate piezometric decline of 4 m caused more than 80 cm of subsidence at borehole 7, whereas a greater piezometric drop of 4 to 17 m led to smaller subsidences (40-70 cm) in the area of boreholes 2, 3 and 4. The estimated storage in the middle of the main subsidence bowl around borehole 7 was greater than around its neighbouring boreholes. The average estimated coefficient around the city of Rafsanjan (borehole 1) was roughly approximately 0.06.

The observed variability in the estimated storage coefficients is related to spatial variations in the soil structures and the thickness of the compressible layers such as clay and silt in different parts of the aquifer. The exemplary lithologic logs in Fig. 2 also indicate the heterogeneity of the aquifer structure. Geotechnical and pumping tests carried out in 1971 close to the locations of piezometers 3 (well 2 in Fig. 3) and 15 (well 1 in Fig. 3) produced a local storage coefficient of 0.0026 and a mean storage coefficient of 0.05 for the whole region (Zayandehroodi, 2012). Our InSAR-based

estimates of the storage coefficient at piezometers 3 and 15 ($S_k \sim 0.05$, Fig. 17) are one order of magnitude larger than the estimates in 1971, although they are close to the mean storage coefficient of the region. Our S_k values are also larger than those expected for elastic deformation in confined aquifers, ranging from approximately 10^{-5} to 10^{-3} (Heath, 1983). Storage coefficients for aquifers characterized by inelastic behaviour are often up to two orders of magnitude higher than those of elastic aquifers (Hoffmann et al., 2001). The lithology close to piezometer 3 (well 2 in Fig. 3) is composed of a 54 m thickness clay unit that is underlain by 88 metres of gravel. The lithology around piezometer 15 shows even thicker layer (> 100 m) of fine-grained silt and clay sediments. The larger estimates for Sk derived from our InSAR and in situ observations can be attributed to the inelastic compaction of low-permeability layers of silt and clay as a consequence of the 18 and 46 m groundwater level drop that has occurred since 1971 at piezometers 15 and 3, respectively.

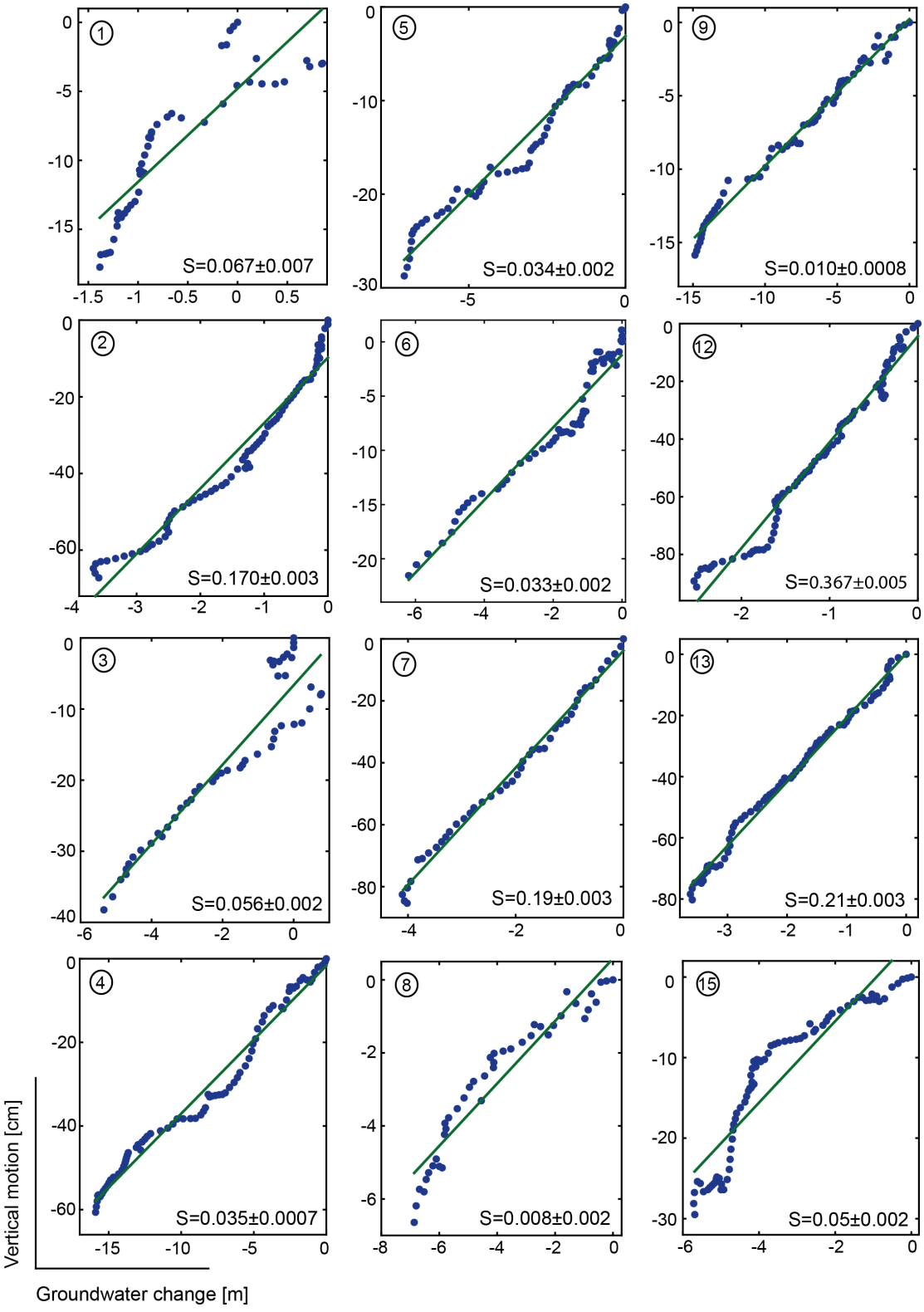

Figure 17: Calculation of storage coefficients from the stress displacement analysis (Riley, 1969). The slopes of the solid lines represent least-squares estimates of the storage coefficient, with 3-sigma uncertainties.

After estimating the storage coefficients at the piezometric wells, we were able to evaluate the storage volume changes between the years 2004-2010 using the method described in Section 3.2. Assuming a mean storage coefficient for the entire aquifer of $\bar{S} \sim 0.1$ (average of all the storage coefficients in Fig. 17), the overall area of the aquifer as A ~ 4108 km^2 (Jaghdani and Brummer, 2011), and the overall groundwater level change between the years 2004-2010 as $\Delta h = -4.62\ m$ (Fig. 4), the storage-volume loss for the above period was estimated as 1897 mcm, which corresponds to an average volume storage loss of approximately 300 mcm per year.

5. Conclusions

Using SAR data from the Envisat, ALOS and Sentinel-1 satellites, we analysed nearly a decade of land subsidence in the Rafsanjan region in Iran. An InSAR time-series analysis showed a persistent pattern of subsidence, with peak values found west of the city of Rafsanjan in the Noogh-Bahreman and Koshkoueieh-Rafsanjan valleys, where the subsidence rates exceeded 30 cm/yr during the 2000s, affecting and degrading large parts of the agricultural lands. The rates of subsidence appear to be decreasing in recent years, although the extent of the areas affected by subsidence largely remain the same. A general correlation between the rate of subsidence and the groundwater level decline was found. This decline has led to a reduction in pore pressure in the aquifer system, which at the end is responsible for the widely observed subsidence. In areas close to the Quaternary faults, strong differential displacements can be seen in the InSAR results. Field surveys and geological analysis revealed a diffuse 200-300 m wide zone of recently developed shallow (< 3-4 m deep) tension cracks and gully erosion features; their formation and orientation seem to be partly influenced by regional tectonics. By combined an analysis of InSAR-derived deformation rates and groundwater level data, storage coefficients ranging from 8.0×10^{-3} to 0.3 could be estimated for the subsidence

662 area, indicating an inelastic and non-recoverable deformation of the aquifer system in
663 the Rafsanjan valley. This inelastic compression of sediments degrades the aquifer
664 system and poses a challenge for future groundwater availability and remediation
665 measures. These results show that the presented remote sensing-based observations
666 form an important prerequisite for evaluating the degree of degradation of the aquifer
667 system in its relation to the currently ongoing groundwater management. Our findings
668 can help in determining the hazard of further degradation of the aquifers as well as the
669 arable land that is a consequence of the ongoing surface subsidence. Future research
670 should focus on using the obtained results for improved modelling of regional
671 groundwater flow and aquifer system compaction related to the groundwater
672 exploitation schemes. A better understanding of the compaction mechanics occurring
673 in the aquifer system of the Rafsanjan region would open up new opportunities for a
674 more sustainable management of the water resources. In this context, spatio-temporal
675 analysis based on long-term regular InSAR monitoring can provide valuable
676 information about the response of the aquifer to changes in the exploitation schemes
677 and remediation measures such as importing surface water supplies with the goal of the
678 recovery of the largely compacted aquifers. The recently launched Sentinel-1 SAR
679 mission, which covers large areas (Swath width ~ 250 km) with high temporal
680 resolution (6 days) has opened up new opportunities for the large-scale and continuous
681 monitoring of surface deformation related to groundwater exploitation, including
682 economically capturing 2D displacement fields in near real-time. This will lead to new
683 remote sensing based approaches in evaluating subsidence hazards and related risks for
684 the agricultural use of developed groundwater basins.
685

686 **Acknowledgements**

This work was supported by the Initiative and Networking Fund of the Helmholtz Association in the frame of the Helmholtz Alliance's "Remote Sensing and Earth System Dynamics". ALOS original data is copyright 2013-2018 Japanese Aerospace Exploration Agency and provided under proposal 1162. Envisat SAR data provided by the European Space Agency (ESA) under CAT-1 project ID 31014. We would like to thank the journal Editor, Dr. Janusz Wasowski, and two anonymous reviewers fro their very helpful and insightful comments, which greatly improved the quality of the original manuscript.

References

Abidin, H., Djaja, R., Darmawan, D., Hadi, S., Akbar, A., Rajiyowiryono, H., Sudibyo, Y., Meilano, I., Kasuma, M. A., Kahar, J., and Subarya, C., 2001, Land Subsidence of Jakarta (Indonesia) and its Geodetic Monitoring System. Nat. Hazards. 23 (2-3), 365-387, doi: 310.1023/A:1011144602064.

Abidin, H. Z., Andreas, H., Djaja, R., Darmawan, D., and Gamal, M., 2008, Land subsidence characteristics of Jakarta between 1997 and 2005, as estimated using GPS surveys. GPS Solutions 12(1), 23-32, doi: 10.1007/s10291-10007-10061-10290.

Aghanabati, A., 2004, Geology of Iran, Geological survey of Iran (In Persian), ISBN: 9646178138, 586 p.

Akbari, V., and Motagh, M., 2012, Improved Ground Subsidence Monitoring Using Small Baseline SAR Interferograms and a Weighted Least Squares Inversion Algorithm. IEEE Geosci. Remote Sens. Lett. 9(3), 437-441, doi: 410.1109/LGRS.2011.2170952.

Amelung, F., Galloway, D. L., Bell, J. W., Zebker, H. A., and Laczniak, R. J., 1999, Sensing the ups and downs of Las Vegas. InSAR reveals structural control of

land subsidence and aquifer-system deformation: Geology 27(6), 483-486, doi: 10.1130/0091-7613(1999)027<0483:STUADO>2.3.CO;2.

Anderssohn, J., Wetzel, H.-U., Walter, T. R., Motagh, M., Djamour, Y., and Kaufmann, H., 2008, Land subsidence pattern controlled by old alpine basement faults in the Kashmar Valley, northeast Iran: results from InSAR and levelling. Geophys. J. Int. 174 (1), 287-294, doi: 210.1111/j.1365-1246X.2008.03805.x.

Bawden, G. W., Thatcher, W., Stein, R. S., Hudnut, K. W., and Peltzer, G., 2001, Tectonic contraction across Los Angeles after removal of groundwater pumping effects. Nature 412 (6849), 812-815, doi:810.1038/35090558.

Bell, J. W., Amelung, F., Ramelli, A. R., and Blewitt, G., 2002, Land Subsidence in Las Vegas, Nevada, 1935-2000: New Geodetic Data Show Evolution, Revised Spatial Patterns, and Reduced Rates. Environ. Eng. Geosci. 8 (3), 155-174, doi: 110.2113/2118.2113.2155.

Berardino, P., Costantini, M., Franceschetti, G., Iodice, A., Pietranera, L., and Rizzo, V., 2003, Use of differential SAR interferometry in monitoring and modelling large slope instability at Maratea (Basilicata, Italy). Eng. Geol. 68 (1-2), 31-51, doi: 10.1016/S0013-7952(1002)00197-00197.

Berardino, P., Fornaro, G., Lanari, R., and Sansosti, E., 2002, A new algorithm for surface deformation monitoring based on small baseline differential SAR interferograms. IEEE Trans. Geosci. Remote Sens. 40 (11), 2375–2383, doi: 2310.1016/S0013-7952(2302)00197-00197.

Bundschuh, J., 2010, Introduction to the numerical modeling of groundwater and geothermal systems: fundamentals of mass, energy and solute transport in poroelastic rocks, CRC Press, ISBN: 0415404231.

736 Burbey, T. J., 2008, The Influence of Geologic Structures on Deformation due to
737 Ground Water Withdrawal. Ground Water 46 (2), 202-211, doi:
738 210.1111/j.1745-6584.2007.00395.x.
739 Cabral-Cano, E., Dixon, T. H., Miralles-Wilhelm, F., Díaz-Molina, O., Sánchez-
740 Zamora, O., and Carande, R. E., 2008, Space geodetic imaging of rapid ground
741 subsidence in Mexico City. Geol. Soc. Am. Bull. 120 (11-12), 1556-1566, doi:
742 1510.1130/b26001.26001.
743 Calderhead, A. I., Therrien, R., Rivera, A., Martel, R., and Garfias, J., 2011, Simulating
744 pumping-induced regional land subsidence with the use of InSAR and field data
745 in the Toluca Valley, Mexico. Adv. Water Resour. 34 (1), 83-97, doi:
746 10.1016/j.advwatres.2010.1009.1017.
747 Canova, F., Tolomei, C., Salvi, S., Toscani, G., and Seno, S., 2012, Land subsidence
748 along the Ionian coast of SE Sicily (Italy), detection and analysis via Small
749 Baseline Subset (SBAS) multitemporal differential SAR interferometry. Earth
750 Surface Processes and Landforms 37 (3), 273-286, doi: 210.1002/esp.2238.
751 Casu, F., Manzo, M., and Lanari, R., 2006, A quantitative assessment of the SBAS
752 algorithm performance for surface deformation retrieval from DInSAR data.
753 Remote Sens. of Environ. 102 (3), 195-210, doi:
754 110.1016/j.rse.2006.1001.1023.
755 Chen, C.-T., Hu, J.-C., Lu, C.-Y., Lee, J.-C., and Chan, Y.-C., 2007, Thirty-year land
756 elevation change from subsidence to uplift following the termination of
757 groundwater pumping and its geological implications in the Metropolitan Taipei
758 Basin, Northern Taiwan. Eng. Geol. 95 (1–2), 30-47, doi:
759 10.1016/j.enggeo.2007.1009.1001.

760 Chen, M., Tomás, R., Li, Z., Motagh, M., Li, T., Hu, L., Gong, H., Li, X., Yu, J., and
761 Gong, X., 2016, Imaging Land Subsidence Induced by Groundwater Extraction
762 in Beijing (China) Using Satellite Radar Interferometry. Remote Sens. 8 (6),
763 doi: 10.3390/rs8060468.
764 Conway, B. D., 2015, Land subsidence and earth fissures in south-central and southern
765 Arizona, USA. Hydrogeol. J., doi: 10.1007/s10040-10015-11329-z.
766 Davoodijam, M., Motagh, M., and Momeni, M., Land Subsidence in Mahyar Plain,
767 Central Iran, Investigated Using Envisat SAR Data, *in* Proceedings The 1st
768 International Workshop on the Quality of Geodetic Observation and Monitoring
769 Systems (QuGOMS'11)2015, Springer, 127-130, doi: 110.1007/1978-1003-
770 1319-10828-10825_10818.
771 Dehghani, M., Valadan Zoej, M. J., Entezam, I., Mansourian, A., and Saatchi, S., 2009,
772 InSAR monitoring of progressive land subsidence in Neyshabour, northeast
773 Iran. Geophys. J. Int. 178 (1), 47-56, doi: 10.1111/j.1365-1246X.2009.04135.x.
774 Dehghani, M., Zoej, M. J. V., and Entezam, I., 2013, Neural Network Modelling of
775 Tehran Land Subsidence Measured by Persistent Scatterer Interferometry:
776 Photogrammetrie-Fernerkundung-Geoinformation, 2013 (1), 5-17, doi:
777 10.1127/1432-8364/2013/0154.
778 Dixon, T. H., Amelung, F., Ferretti, A., Novali, F., Rocca, F., Dokka, R., Sella, G.,
779 Kim, S.-W., Wdowinski, S., and Whitman, D., 2006, Space geodesy:
780 Subsidence and flooding in New Orleans. Nature, 441 (7093), 587-588, doi:
781 510.1038/441587a.
782 Ezquerro, P., Herrera, G., Marchamalo, M., Tomás, R., Béjar-Pizarro, M., and
783 Martínez, R., 2014, A quasi-elastic aquifer deformational behavior: Madrid

784 aquifer case study. J. Hydrol. 519 (A), 1192-1204, doi:
785 1110.1016/j.jhydrol.2014.1108.1040.
786 Farr, T. G., and Kobrick, M., 2000, Shuttle Radar Topography Mission produces a
787 wealth of data. Eos Trans. Am. Geophys. Un. 81, 583-585, doi:
788 510.1029/EO1081i1048p00583.
789 Fattahi, H., Agram, P., and Simons, M., 2016, A Network-Based Enhanced Spectral
790 Diversity Approach for TOPS Time-Series Analysis. EEE Trans. Geosci.
791 Remote Sens. doi: 10.1109/TGRS.2016.2614925.
792 Ferretti, A., Prati, C., and Rocca, F., 2001, Permanent Scatterers in SAR Interferometry.
793 IEEE Trans. Geosci. Remote Sens. 39 (1), 8-20, doi: 10.1029/2006GL028189.
794 Ferretti, A., Savio, G., Barzaghi, R., Borghi, A., Musazzi, S., Novali, F., Prati, C., and
795 Rocca, F., 2007, Submillimeter accuracy of InSAR time series: Experimental
796 validation. IEEE Trans. Geosci. Remote Sens. 45 (5), 1142-1153, doi:
797 1110.1109/TGRS.2007.894440.
798 Galloway, D. L., and Burbey, T. J., 2011, Review: regional land subsidence
799 accompanying groundwater extraction. Hydrogeol. J. 19 (8), 1459-1486, doi:
800 1410.1007/s10040-10011-10775-10045.
801 Galloway, D. L., and Hoffmann, J., 2007, The application of satellite differential SAR
802 interferometry-derived ground displacements in hydrogeology. Hydrogeol. J.
803 15 (1), 133-154, doi: 110.1007/s10040-10006-10121-10045.
804 Galloway, D. L., Hudnut, K. W., Ingebritsen, S. E., Phillips, S. P., Peltzer, G., Rogez,
805 F., and Rosen, P. A., 1998, Detection of Aquifer System Compaction and Land
806 Subsidence Using Interferometric Synthetic Aperture Radar, Antelope Valley,
807 Mojave Desert, California. Water Resour. Res. 34, 2573-2585, doi:
808 2510.1029/2598wr01285.

809 Geudtner, D., Torres, R., Snoeij, P., Davidson, M., and Rommen, B., Sentinel-1 System
810 capabilities and applications, *in* Proceedings IGARSS2014, p. 1457-1460.
811 Ghorbani, M., 2013, The economic geology of Iran: mineral deposits and natural
812 resources, Springer Science & Business Media, ISBN: 978-94-007-5625-0.
813 Heath, R. C., 1983, Basic ground-water hydrology.
814 Herrera, G., Fernández, J. A., Tomás, R., Cooksley, G., and Mulas, J., 2009, Advanced
815 interpretation of subsidence in Murcia (SE Spain) using A-DInSAR data–
816 modelling and validation. Nat. Hazards Earth Syst. Sci. 9 (3), 647-661, doi:
817 610.5194/nhess-5199-5647-2009.
818 Hessami, K., Jamali, F., and Tabassi, H., 2003, Major Active Faults of Iran,
819 Map1:2,500,000: International Institute of Earthquake Engineering and
820 Seismology (IIEES), Tehran.
821 Hoffmann, J., Galloway, D. L., and Zebker, H. A., 2003, Inverse modeling of interbed
822 storage parameters using land subsidence observations, Antelope Valley,
823 California. Water Resour. Res. 39, doi: 10.1029/2001wr001252.
824 Hoffmann, J., Zebker, H. A., Galloway, D. L., and Amelung, F., 2001, Seasonal
825 Subsidence and Rebound in Las Vegas Valley, Nevada, observed by Synthetic
826 Aperture Radar Interferometry. Water Resour. Res. 37 (6), 1551-1566, doi:
827 1510.1029/2000WR900404.
828 Holzer, T. L., and Pampeyan, E. H., 1981, Earth fissures and localized differential
829 subsidence. Water Resour. Res. 17 (1), 223-227, doi:
830 210.1029/WR1017i1001p00223.
831 Hooper, A., 2008, A multi-temporal InSAR method incorporating both persistent
832 scatterer and small baseline approaches. Geophys. Res. Lett. 35,
833 doi:10.1029/2008GL034654.

834 Hooper, A., Zebker, H., Segall, P., and Kampes, B., 2004, A new method for measuring
835 deformation on volcanoes and other natural terrains using InSAR persistent
836 scatterers. Geophys. Res. Lett., 31 (23), doi: 23610.21029/22004gl021737.
837 Hooper, A., and Zebker, H. A., 2007, Phase unwrapping in three dimensions with
838 application to InSAR time series. J. Opt. Soc. Am. A. 24 (9), 2737-2747, doi:
839 2710.1364/JOSAA.2724.002737.
840 Huang, B., Shu, L., and Yang, Y. S., 2012, Groundwater Overexploitation Causing
841 Land Subsidence: Hazard Risk Assessment Using Field Observation and Spatial
842 Modelling. Water Resour. Manag. 26 (14), 4225-4239, doi: 4210.1007/s11269-
843 11012-10141-y.
844 Hung, W.-C., Hwang, C., Liou, J.-C., Lin, Y.-S., and Yang, H.-L., 2012, Modeling
845 aquifer-system compaction and predicting land subsidence in central Taiwan.
846 Eng. Geol. 147, 78-90, doi: 10.1016/j.enggeo.2012.1007.1018.
847 Jaghdani, T. J., and Brummer, B., Demand for Irrigation Water for Pistachio Production
848 from Depleting Groundwater Resources: Spatial Econometric Approach, *in*
849 Proceedings 2011 International Congress, August 30-September 2, 2011,
850 Zurich, Switzerland, European Association of Agricultural Economists.
851 Kampes, B., Hanssen, R., and Perski, Z., Radar Interferometry with Public Domain
852 Tools, *in* Proceedings Fringe 2003, Available online at:
853 http://earth.esa.int/fringe03/proceedings/papers/22_kampes.pdf (accessed 6
854 January 2017).
855 Kim, J.-W., Lu, Z., Jia, Y., and Shum, C., 2015, Ground subsidence in Tucson, Arizona,
856 monitored by time-series analysis using multi-sensor InSAR datasets from 1993
857 to 2011. ISPRS J. Photogramm. Remote Sens. 107, 126-141, doi:
858 110.1016/j.isprsjprs.2015.1003.1013.

859 Lu, Z., and Danskin, W. R., 2001, InSAR Analysis of Natural Recharge to Define
860 Structure of a Ground-Water Basin, San Bernardino, California. Geophys. Res.
861 Lett. 28, 2661-2664, doi: 2610.1029/2000GL012753
862 Mahdavi, M. A., Nazer, N.H., Aghanabati, A., Soheili. M.,Mohajel , M.,Haj Mola Ali,
863 A., 1996, Geological map - 1:250 000, sheet NH 40.2- Ravar: Geological
864 Survey of Iran, 250000.
865 Manzo, M., Fialko, Y., Casu, F., Pepe, A., and Lanari, R., 2012, A quantitative
866 assessment of DInSAR measurements of interseismic deformation: the
867 Southern San Andreas Fault case study. Pur. Appl. Geophys. 169 (8), 1463-
868 1482, doi: 1410.1007/s00024-00011-00403-00022.
869 Mehryar, S., Sliuzas, R., Sharifi, A., and van Maarseveen, M., 2015, The water crisis
870 and socio-ecological development profile of Rafsanjan Township, Iran:
871 Management of Natural Resources, Sustainable Development and Ecological
872 Hazards IV, 199, 271-282, ISSN: 1743-3541.
873 Motagh, M., Walter, T. R., Sharifi, M. A., Fielding, E., Schenk, A., Anderssohn, J., and
874 Zschau, J., 2008, Land subsidence in Iran caused by widespread water reservoir
875 overexploitation. Geophys. Res. Lett. 35, doi: 10.1029/2008GL033814.
876 Motagh, M., Djamour, Y., Walter, T. R., Wetzel, H-U. Zschau, J., and Arabi, S., 2007,
877 Land subsidence in Mashhad Valley, northeast Iran: results from InSAR,
878 levelling and GPS. Geophys. J. Int. 168 (2), 518-526, doi: 510.1111/j.1365-
879 1246X.2006.03246.x.
880 Motagh, M. Shamshiri, R., Haghshenas-Haghighi, M. Wetzel, H-U., Akbari, B.,
881 Nahavandchi, H., Roessner, S., Arabi, S., 2017, Supplement to: Quantifying
882 groundwater exploitation induced subsidence in the Rafsanjan Plain,

883 southeastern Iran, using InSAR time-series and in situ measurements. GFZ Data
884 Services. http://doi.org/10.5880/GFZ.1.4.2017.001
885 Mousavi, S. M., Shamsai, A., Naggar, M. H. E., and Khamehchian, M., 2001, A GPS-
886 based monitoring program of land subsidence due to groundwater withdrawal
887 in Iran. Can. J. Civ. Eng. 28 (3), 452-464, doi: 410.1139/l1101-1013.
888 Phien-wej, N., Giao, P. H., and Nutalaya, P., 2006, Land subsidence in Bangkok,
889 Thailand. Eng. Geol. 82 (4), 187-201, doi: 110.1016/j.enggeo.2005.1010.1004.
890 Prats-Iraola, P., Scheiber, R., Marotti, L., Wollstadt, S., and Reigber, A., 2012, TOPS
891 interferometry with TerraSAR-X. IEEE Trans. Geosci. Remote Sens. 50(8),
892 3179-3188, doi: 3110.1109/TGRS.2011.2178247.
893 Rahnama, M. B., and Moafi, H., 2009, Investigation of land subsidence due to
894 groundwater withdraw in Rafsanjan plain using GIS software. Arab. J. Geosci.
895 2(3), 241-246, doi: 210.1007/s12517-12009-10034-12514.
896 Rigo, A., Béjar-Pizarro, M., and Martínez-Díaz, J., 2013, Monitoring of Guadalentín
897 valley (southern Spain) through a fast SAR Interferometry method. J. Appl.
898 Geophys. 91, 39-48.
899 Riley, F. S., 1969, Analysis of borehole extensometer data from central California.
900 Land Subsidence, 2, 423-431.
901 Samieie-Esfahany, S., Hanssen, R., van Thienen-Visser, K., and Muntendam-Bos, A.,
902 On the effect of horizontal deformation on InSAR subsidence estimates, *in*
903 Proceedings Proceedings of The Fringe 2009 Workshop, Frascati, Italy2009,
904 Volume 30.
905 Samsonov, S., and d'Oreye, N., 2012, Multidimensional time-series analysis of ground
906 deformation from multiple InSAR data sets applied to Virunga Volcanic

907 Province. Geophys. J. Int. 191(3), 1095-1108, doi: 1010.1111/j.1365-
908 1246X.2012.05669.x.
909 Sayyaf, M., Mahdavi, M., Barani, O. R., Feiznia, S., and Motamedvaziri, B., 2014,
910 Simulation of land subsidence using finite element method: Rafsanjan plain
911 case study. Nat. Hazards. 72(2), 309-322, doi: 310.1007/s11069-11013-11010-
912 11066.
913 Scheiber, R., and Moreira, A., 2000, Coregistration of interferometric SAR images
914 using spectral diversity. IEEE Trans. Geosci. Remote Sens. 38 (5), 2179-2191,
915 doi: 2110.1109/2136.868876.
916 Shamshiri, R., Motagh, M., Baes, M., and Sharifi, M., 2014, Deformation analysis of
917 the Lake Urmia causeway (LUC) embankments in northwest Iran: insights from
918 multi-sensor interferometry synthetic aperture radar (InSAR) data and finite
919 element modeling (FEM). J. Geodesy. 88(12), 1171-1185, doi:
920 1110.1007/s00190-00014-00752-00196.
921 Stramondo, S., Saroli, M., Tolomei, C., Moro, M., Doumaz, F., Pesci, A., Loddo, F.,
922 Baldi, P., and Boschi, E., 2007, Surface movements in Bologna (Po Plain —
923 Italy) detected by multitemporal DInSAR. Remote Sens. Environ. 110 (3),
924 304-316, doi: 310.1016/j.rse.2007.1002.1023.
925 Teatini, P., Tosi, L., Strozzi, T., Carbognin, L., Wegmüller, U., and Rizzetto, F., 2005,
926 Mapping regional land displacements in the Venice coastland by an integrated
927 monitoring system. Remote Sens. Environ. 98 (4), 403-413, doi:
928 410.1016/j.rse.2005.1008.1002.
929 Terzaghi, K., 1925, Principles of soil mechanics, IV—Settlement and consolidation of
930 clay: Engineering News-Record, 95 (3), 874-878.

931 Tomás, R., Herrera, G., Delgado, J., Lopez-Sanchez, J. M., Mallorquí, J. J., and Mulas,
932 J., 2010a, A ground subsidence study based on DInSAR data: Calibration of
933 soil parameters and subsidence prediction in Murcia City (Spain). Eng. Geol.
934 111(1–4), 19-30, doi: 10.1016/j.enggeo.2009.1011.1004.
935 Tomás, R., Herrera, G., Lopez-Sanchez, J., Vicente, F., Cuenca, A., and Mallorquí, J.,
936 2010b, Study of the land subsidence in Orihuela City (SE Spain) using PSI data:
937 distribution, evolution and correlation with conditioning and triggering factors.
938 Eng. Geol. 115 (1), 105-121, doi: 110.1016/j.enggeo.2010.1006.1004.
939 Tosi, L., Teatini, P., and Strozzi, T., 2013, Natural versus anthropogenic subsidence of
940 Venice. Scientific Reports, 3, doi: 2710.1038/srep02710.
941 Tung, H., Chen, H.-Y., Hu, J.-C., Ching, K.-E., Chen, H., and Yang, K.-H., 2016,
942 Transient deformation induced by groundwater change in Taipei metropolitan
943 area revealed by high resolution X-band SAR interferometry. Tectonophysics,
944 doi: 10.1016/j.tecto.2016.03.030.
945 Wegmuller, U., and Werner, C., 1997, Gamma SAR processor and interferometry
946 software, The 3rd ERS symposium on space at the service of our environment,
947 Florence, Italy, 1687-1692.
948 Yagüe-Martínez, N., Prats-Iraola, P., Gonzalez, F. R., Brcic, R., Shau, R., Geudtner,
949 D., Eineder, M., and Bamler, R., 2016, Interferometric Processing of Sentinel-
950 1 TOPS Data. IEEE Trans. Geosci. Remote Sens. 54 (4), 2220-2234, doi:
951 2210.1109/TGRS.2015.2497902.
952 Zayandehroodi, 2012, Report on Recommendations for further restrictions on
953 groundwater resources in Rafsanjan (In Persian).
954 Zohrehbakhsh A., Vahdati Daneshmand F., Srdic A., Dimitrijevic M. N., Djokovis I.
955 N., Lotfi M., Haghipour A., Sabzehei M., Behroozi A., Lescuyer J., and Riou,

R., 1992, Geological quadrangle map of Rafsanjan, scale 1:250 000: Geological Survey of Iran.